MICROCOPY RESOLUTION TEST CHART
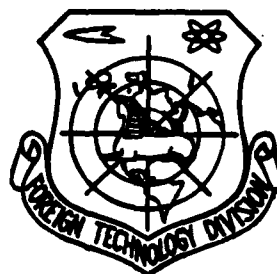
NATIONAL BUREAU OF STANDARDS - 1963 - A

FOREIGN TECHNOLOGY DIVISION

ACTA AERODYNAMICS SINICA

(SELECTED ARTICLES)

DTIC

ELECTE

DEC 18 1985

S D

D

DTIC FILE COPY

85 12 17 029

EDITED TRANSLATION

FTD-ID(RS)T-0493-85   22 Nov 85

MICROFICHE NR: FTD-85-C-001167

ACTA AERODYNAMICS SINICA (SELECTED ARTICLES)

English pages: 91

Source: Zhongguo Quiliu Dongli Xue, Nr. 2,
        1984, pp. 19-40; 66-72; 78-82; 87-92

Country of origin: China
Translated by: SCITRAN
               F33657-84-D-0165
Requester: FTD/TQTA
Approved for public release; distribution unlimited.

Table of Contents

i

GRAPHICS DISCLAIMER

All figures, graphics, tables, equations, etc. merged into this
translation were extracted from the best quality copy available.

A Fast Algorithm of the Finite Difference Method for the

Computation of the Transonic Flow Past an Arbitrary Airfoil

with the Conservation of the Full Potential Equation

Huang Mingke

(Nanjing Aeronautical Institute)

I.   Introduction

There are two primary finite difference methods to solve the full potential equation for the transonic flow around an airfoil. One of them was developed by Garabedian, Korn and Jameson[1][2]. This method first conformally maps the exterior of the airfoil on the physical plane onto the interior of a circle. Then, a fast direct method and a linear relaxation technique are used in the circle to solve the full potential finite difference equation. Because the center of the circle corresponds to infinity on the physical plane, the velocity potential is infinite at that point. In order to avoid this singularity, Jameson introduced the perturbation potential to eliminate the free flow velocity potential which includes such singularity to complicate the governing equation. The other method was developed by Holst[3]. He used an arbitrary curve coordinate which matches the surface to transform the computation zone into a rectangle. Then, the AF_2 iteration scheme is used to solve the finite difference equation in the rectangular region. AF_2 is a fast and effective iteration scheme which has already been widely used[4]-[6]. Because Holst used an arbitrary non-orthogonal curved coordinate, it is highly

1

flexible. However, it takes some computer time to create such a
mesh. In addition, the equation becomes more complex after the
transformation.

On the basis of these two methods, a simpler method is
developed in this work. We first employ conformal mapping to
transform the computing region into a unit circle. Then, a
radial transformation is carried out in the circle to reduce the
effect of singularity of velocity potential at the center of the
circle. Hence, it is not necessary to introduce the perturbation
potential. The governing function is thus much simpler than
those used by Jameson and Holst. Then, the equation of
conservation of full potential is discretized using a center
difference scheme. Moreover, an artificial density is introduced
to the artificial viscosity in the supersonic region[3],[7].
Finally, the finite difference equation is solved by the AF_2
scheme developed by Holst. A computer program has already been
written for this algorithm. Computations have already proven
that this algorithm is successful and effective.

II. Computation Method

First, the exterior profile of the airfoil on the complex
physical z-plane is mapped onto the unit circle σ by conformal
mapping. The derivative of the transformation function is[2],[8]

$$\frac{dz}{d\sigma} = \left(1 - \frac{1}{\sigma}\right)^{\cdots} \exp \sum_{i=1}^{N} \frac{c_i}{\sigma^i} \qquad (1)$$

2

where ϵ is the trailing edge angle of the airfoil. Let $\sigma = e^{-i\theta}$ /20 /r and $\theta = 0$ corresponds to the trailing edge of the airfoil. This transformation is able to map an open trailing edge onto an enclosed circle. The coefficient c_n in equation (1) needs to be determined by iteration[8], usually by 7-8 iterations. Because the fast Fourier transform (FFT) technique is used in the iteration, the conformal mapping process takes less than a half minute on a TQ-16 computer. Then, it is transformed according to $\xi=1/\sigma$ to map from outside onto the inside of the unit circle. Therefore, r, θ and ξ are the polar coordinates on the plane.

The velocity and velocity components are rendered undimensional by using the critical sonic speed. The density is made dimensionless with the value at the stationary point. The conservative full potential equation on the ξ plane thus becomes

$$\frac{\partial}{\partial \theta}\left(\frac{\rho}{r}\frac{\partial \phi}{\partial \theta}\right)+\frac{\partial}{\partial r}\left(\rho r\frac{\partial \phi}{\partial r}\right)=0 \qquad (2)$$

where ϕ is the velocity potential. The velocity components U and V along the θ and r coordinates on the physical plane can be expressed as

$$U=\frac{r}{H}\frac{\partial \phi}{\partial \theta}, \qquad V=\frac{r'}{H}\frac{\partial \phi}{\partial r} \qquad (3)$$

where $H = |dz/d\sigma|$ is the transformation mode. The relation between ρ and the velocity components is:

$$\rho=\left[1-\frac{\gamma-1}{\gamma+1}(U'+V')\right]^{\frac{1}{\gamma-1}} \qquad (4)$$

3

where γ is the specific heat. The boundary conditions on the ξ plane are

Along the surface $(\partial\phi/\partial r)_{r=1}=0$ (5)

At infinity or when r→ 0,

$$\phi \to V_\infty \frac{\cos(\alpha+\theta-\mu)}{r} + \frac{\Gamma}{2\pi} \tan^{-1}[(1-M_\infty^2)^{1/2}\tan(\theta+\alpha-\mu)] \qquad (6)$$

where V_∞ and M_∞ are the incident velocity and Mach number of the flow. α is the angle of attack and μ is the imaginary part of the coefficient c_0, which corresponds to the zero attack angle of the airfoil at low velocities. This can ensure that the conformal mapping is defined. Γ is the ring around the airfoil, which is determined by the Kutta condition. The Kutta condition requires that $(\partial\phi/\partial\theta)_{\theta=0} = 0$.

From equation (6) we find that $\phi \sim (1/r)$ near the origin. Therefore, the boundary conditions cannot be directly written for r=0. However, it is possible to choose the external boundary on the physical plane at a far away location[9] and the flow parameters there are considered as the free flow values. If the external boundary conditions are rewritten on the ξ plane at $r=r_{min}$ where r_{min} is very small, because the radial step Δr in the finite difference method may be of the same order of magnitude as r_{min}, the finite difference of approximation of the derivative $\partial\phi/\partial r$ has a very large error near r_{min}. For this reason, Jameson introduced a perturbation potential to overcome this difficulty. We employ the following radial transformation

4

$$r = [m-(m-1)R]R^m \qquad (7)$$

Figure 1 shows several r vs. R curves at different m values.
These curves intersect the R-axis at the origin. They intersect
the straight line r=R at R=1. The following computation, we
choose m=6 and R_{min}=0.5, corresponding to r_{min}=0.0547 or to the
fact that the external boundary of the physical plane is
approximately 4.6 times chord length from the center. When we
divide the R coordinate into meshes, the step ΔR may be much
smaller than R_{min}. Thus, the above difficulty is overcome.

Equation (2) can be transformed as:

$$\frac{\partial}{\partial\theta}\left(\frac{\rho}{f(R)}\frac{\partial\phi}{\partial\theta}\right) + \frac{\partial}{\partial R}\left(\rho f(R)\frac{\partial\phi}{\partial R}\right) = 0 \qquad (8)$$

where the function   /21

$$f(R) = \left(\frac{m-(m-1)R}{m^2-(m^2-1)R}\right)R \qquad (9)$$

The value at each radial mesh point can be calculated in the
advanced. Therefore, it does not add any complexity to the
governing equation.

Figure 2 shows the physical plane and various transformation
planes. In the physical plane, a seam from the trailing edge of
the airfoil is dividing the computation region into singularly
connecting regions to made the velocity potential singular in it.
The jump of ϕ across the seam is equal to the circular moment.
The computation region in the (R,θ) plane is rectangular. In
order to create the difference lattice, it is divided into i_{max}

5

meshes in the θ-direction and j_{max} meshes in the R-direction. R_{min} corresponds to $j=j_{min}$. Hence, the computation region in the (R, θ)plane corresponds to $0 \leqslant i \leqslant i_{max}+1$ and $j_{min} \leqslant j \leqslant j_{max}$, as shown in Figure 2(c).
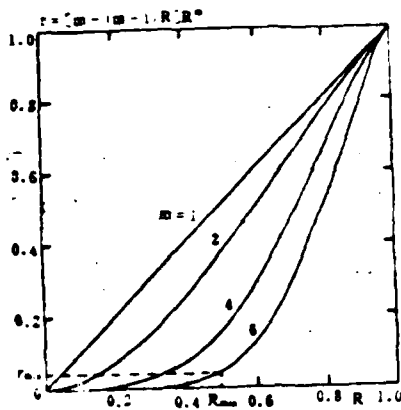
Figure 1. The Radial Coordinate Transformation Function

6
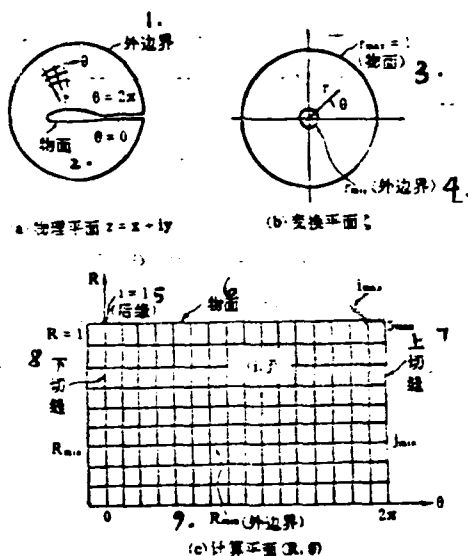
Figure 2. Physical Plane, Transformation Plane and Computation
Plane

     1.   external boundary
     2.   surface
     3.   surface
     4.   external boundary
     5.   trailing edge
     6.   surface
     7.   upper seam
     8.   lower seam
     9.   external boundary
     (a) physical plane z=x+iy
     (b) transformation plane ξ
     (c) computation plane (R,θ)

In analogy to the Holst method[3], the finite difference
approximation of equation (8) is

$$L\phi_{ij} = \vec{\delta}_{\theta} \cdot \left[\left(\frac{\bar{\rho}}{f(R)} \right)_{i+\frac{1}{2},j} \vec{\delta}_{\theta} \phi_{ij} \right] - \vec{\delta}_R [(\rho f(R))_{i,j-\frac{1}{2}} \vec{\delta}_R \phi_{ij}] = 0 \tag{10}$$

where $\vec{\delta}_{\theta}$, $\vec{\delta}_R$ and $\overleftarrow{\delta}_{\theta}$, $\overleftarrow{\delta}_R$ are the forward and backward difference
operators. Because the curved coordinate for conformal mapping
is a coordinate to fit the surface of the object, the streamline

7

direction in the supersonic region is relatively close to the θ-direction. Therefore, we only introduced the artificial viscosity in the θ-direction. To this end, an artificial density[3] $\tilde{\rho}$ is used in equation (10) to replace ρ. We get

$$\tilde{\rho}_{i+\frac{1}{2},j} = (1 - \nu_{i+k,j})\rho_{i+\frac{1}{2},j} + \nu_{i+k,j}\rho_{i+2k-\frac{1}{2},j} \qquad (11)$$

where $\qquad v = \max[0, (M^2-1)c] \qquad (12)$

Here, M is the local Mach number. The coefficient c is between 1-2. Another limit is that the value of v cannot be larger than 1. In equation (11) k is chosen to be

$$k = \left\{ \begin{array}{l} 0 \text{ when } U_{i+\frac{1}{2},j} > 0 \\ 1 \text{ when } U_{i+\frac{1}{2},j} < 0 \end{array} \right.$$

When we calculate the density ρ on a mesh point based on equation (5), the required U and V are calculated by the center difference. The densities with the 1/2 indicator were computed /22 by taking the average. Due to the fact that $\tilde{\rho}=\rho$ in the subsonic region, therefore, the difference approximation equation (10) has a second order accuracy. However, the difference term with respect to θ only has a first order accuracy.

The iteration scheme can be written as[3]

$$NC^n + \omega L\phi^n = 0 \qquad (13)$$

where n is the number of iterations, $C^n = \phi^{n+1} - \phi^n$ is a correction term, $L\phi^n$ is the residual value, and ω is the relaxation factor. The operation N should be selected to be as close to L as possible. It should also facilitate the process to find its

inverse. We chose a two multiplying factor format

$$a \mathcal{N} C_{i,j} = -[a - \bar{\delta}_R (\rho f(R))_{i,j-\frac{1}{2}}] \left[a \bar{\delta}_R - \bar{\delta}_\theta \left(\frac{\bar{\rho}}{f(R)} \right)_{i+\frac{1}{2},j} \bar{\delta}_\theta \right] C_{i,j}$$

where α is the acceleration parameter (not to be confused with the front attack angle).

Each iteration is specifically implemented in two steps:
First step:

$$[a - \bar{\delta}_R (\rho f(R))_{i,j-\frac{1}{2}}] f_{i,j} = a \omega L \phi_{i,j} \qquad (14)$$

Second step:

$$\left[a \bar{\delta}_R \mp a\beta \bar{\delta}_\theta - \bar{\delta}_\theta \left(\frac{\bar{\rho}}{f(R)} \right)_{i+\frac{1}{2},j} \bar{\delta}_\theta \right] C_{i,j} = f_{i,j} \qquad (15)$$

where $f_{i,j}^n$ is an intermediate result. In the first step, it is only necessary to solve two diagonal linear algebraic equation sets for each θ=const. line. To this end, it is also required to specify the boundary conditions for $f_{i,j}^n$. Similar to that in reference [3], it is assumed that $\partial f/\partial R = 0$ along the surface. With the intermediate value $f_{i,j}^n$, it is possible to solve the tridiagonal algebraic equations for each R=const. line from the external boundary inward in the second step. Rigorously, this equation is not a tridiagonal. There is one non-zero element on the upper right side and one on the lower left side[10]. Therefore, the velocity potential in the n+1th iteration is $\phi^{n+1} = \phi^n + C^n$ to complete an iteration. In the second step, $\mp a\beta \bar{\delta}_\theta$ is the term to provide convergence to the ϕ_{si} term in the supersonic region[2].

9

The initial field for iteration is chosen as

$$\phi^0 = V_\infty \left(r + \frac{1}{r} \right) \cos\left(\alpha + \theta - \mu \right) + \frac{\Gamma^0}{2\pi} \tan^{-1} \left[(1 - M_\infty^2)^{1/2} \tan\left(\theta + \alpha - \mu \right) \right]$$

where the first term on the right side is the velocity potential
of an incompressible circulationless flow. The second term is
the circulation part. In this equation, α again represents the
angle of attack. Obviously, with the exception that the
circulation is not yet determined, this initial field has already
satisfied the boundary conditions at the external boundary as
well as those on the surface of the object. The initial
circulation Γ^0 is chosen to make the initial field meet the Kutta
condition. When the attack angle is not too large, we get

$$\Gamma^0 = \frac{\Gamma_{incom}}{(1 - M_\infty^2)^{1/2}} = \frac{4\pi V_\infty \sin\left(\alpha - \mu \right)}{(1 - M_\infty^2)^{1/2}}$$

For an incompressible flow, the initial field chosen is the final
solution. For a subsonic flow, the initial circulation is close
to the final value.

Because the initial field already satisfies the Kutta
condition and the circulationless part of the initial field also
meets the external boundary condition, therefore, the correction
field obtained in each iteration is zero at the external
boundary. In order to determine the correction for circulation,
the correction field is required to satisfy the Kutta condition.
Let us assume that we have already found the following
circulations $\Gamma^n, \Gamma^{n-1}, \Gamma^{n-2} \ldots\ldots$ in earlier iterations. We

estimated r^{n+1} in the north iteration by extrapolation. The increment of circulation is estimated to be

$$\Delta\Gamma_{,}=\omega_{r}(2\Gamma^{\cdot}-3\Gamma^{\cdot-\cdot}+\Gamma^{\cdot\cdot})$$

where ω_r is the low relaxation factor. This circulation increment can be used as an auxiliary relation in solving equation (15):

$$C^{\cdot}_{.,}=C^{\cdot}_{\mathbf{max}^{\cdot},}-\Delta\Gamma_{,}, \quad C^{\cdot}_{\mathbf{max}\cdot,.,}=C^{\cdot}_{.,}-\Delta\Gamma, \qquad /23$$

After solving $C^n_{i,j}$ from equation (15), the circulation of the correction field is

$$\Delta\Gamma=C^{\cdot}_{\mathbf{max}^{\cdot}\mathbf{max}}-C^{\cdot}_{.,\mathbf{max}}$$

Therefore, $r^{n+1}=r^{n}+\Delta\Gamma$, which is used to correct the circulation on the external boundary for the next iteration.

III. Numerical Examples

On the (R,θ) plane, the computation region is divided into 20 meshes along the R-direction, i.e., $j_{max}=40$ and $j_{min}=20$. In the θ-direction, i_{max} is equal to 64 and 128. The acceleration parameter chosen is a geometric sequence formed by 8 numeric values. In each iteration, one of the values in the sequence is used in order. After a complete cycle, it starts all over again. α_1 is used to represent the minimum in the sequence and α_n is the maximum. When α_1 is small, it converges rapidly. If it is too small, the correction in each iteration is too large to lead to the solution to diverge. Therefore, α_1 has a lower limit.

11

The selection of the optimal acceleration parameter must rely on trial computation. In the following example, let us choose $\alpha_1 = 10 \sim 20$ and the ratio of two neighboring numbers in the geometric series α is 1.6. In the initial stage, a smaller α_1 is chosen to accelerate the development of the flow field. In the later stage, α_1 is chosen to be larger to avoid the solution diverging. Other parameters are chosen as follows: $\beta = 0 \sim 1.0$, $\omega = 1.8$, $\omega_r = 0.7 \sim 1.0$, $c = 1$.

Figure 3 shows the calculated pressure distribution on the NACA 0012 airfoil when $M_\infty = 0.63$ and attack angle $\alpha = 2°$. This example belongs to the subcritical case. The mesh chosen is 64 x 20. The result is in agreement with that obtained by using the Holst method with a 149 x 28 mesh[3]. This example needs 123 iterations to obtain the convergent result shown in the figure. In this case, the pressure coefficient does not vary by more than 0.001 over 8 iterations, requiring approximately 35 minutes on the computer.

Figure 4 shows the results obtained with both coarse and fine meshes for the same airfoil when $M_\infty = 0.75$ and $\alpha = 2°$. This is an example of the supercritical case, which requires 277 iterations. When a 128 x 20 mesh is chosen, the result is in total agreement with that of Holst's[3].
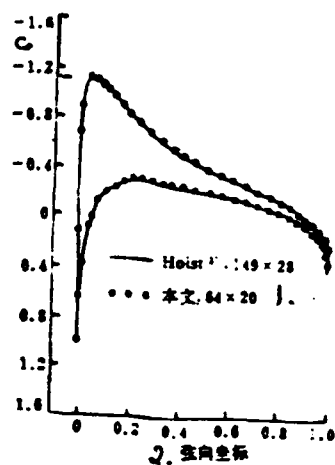
Figure 3. Calculated Results of NACA 0012 Airfoil at $M_\infty=0.63$
and $\alpha = 2°$ Using a Coarse Mesh (64x20)
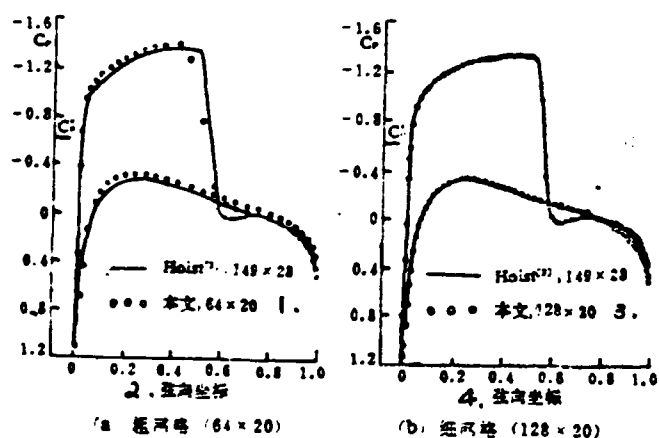
1. this work
2. chord direction coordinate

Figure 4. Calculated Pressure Distribution on NACA 0012 Airfoil
at $M_\infty=0.75$ and $\alpha=2°$

13

(a) coarse mesh (64x20)
(b) fine mesh (128x20)

1. this work
2. chord coordinate
3. this work
4. chord coordinate

All the above computations were done on Chinese made 709 and   /24

TQ-16 computers. It should be pointed out that these

computations were made by choosing the acceleration parameter and

other parameters conservatively because of insufficient computer

time. Preliminary computation already demonstrated that these

parameters have an extremely large effect on the rate of

convergence. Therefore, there is a large potential to accelerate

the process.

References

[1] Garabedian, P.R. and Korn, D.G., Comm. on Pure and Applied
     Math., 24, (1971), 841-851.

[2] Jameson, A., Symposium Transsonicum II, (1975).

[3] Holst, T.L., AIAA Journal, 17, 10, (1979), 1038-1045.

[4] Holst, T.L., AIAA Journal, 18, 12, (1980), 1431-1439.

[5] Catherall, D., AIAA Paper 81-1018.

[6] Baker, T.J. and Forsey, C.R., AIAA Paper 81-1015.

[7] Hafez, M.M., Murman, E.M. and South, J.C., AIAA Paper
     78-1148.

[8] Bauer, F. and Korn, D., AIAA 2nd Computational Fluid
     Dynamics Conference, (1975).

[9] Steger, J.L. and Lomax, H., AIAA Journal, 10, 1, (1972),
     49-54.

[10] Holst, T.L., Private Communication, July 31, (1981).

A FAST ALGORITHM OF THE FINITE DIFFERENCE METHOD FOR COMPUTATION OF THE TRANSONIC FLOW PAST AN ARBITRARY AIRFOIL WITH THE CONSERVATIVE FULL–POTENTIAL EQUATION

Huang Mingke

(Nanjing Aeronautical Institute)

Abstract

Based on the methods developed by Jameson and Holst, a computer program has been developed for computation of the transonic flow past an arbitrary airfoil by the finite difference method. A conformal mapping is applied to map the exterior of the airfoil onto the interior of a circle. By a radial transformation reducing the effects of the singularity at the centre of the circle, the use of the perturbation velocity potential is avoided. The governing equation simpler than those used by Jameson and Holst is approximated by a finite difference equation, which is then solved by AF2 iteration scheme in computing plane. The computations of the pressure distribution over the airfoil of NACA 0012 for subcritical and supercritical cases show the results in excellent agreement with those. by Holst's method.

A Mixed Finite Difference Analysis of the Internal and External Transonic Flow Fields of Center Cone Inlet

Luo Shijun, Shen Huili, Ji Minggang and Xing Zongwen

(Northwestern Polytechnical University)

and

Dong Songye and Han Aiqing

(31th Institute, Ministry of Astronautical Industry)

I.   Introduction

In reference [1], the internal and external transonic flow field of a Pitot tube type axisymmetric inlet was successfully calculated by applying a mixed finite difference method to the transonic steady potential of the flow. The shape of a center cone gas inlet mostly belongs to the contraction-expansion type. The disturbance on the internal wall surface is relatively intense. In addition, due to the presence of the centerbody, the transversal relaxation line which is able to transmit outlet resistance against pressure disturbance is cut off. Therefore, the alternating direction linear relaxation iteration technique used in the calculation of a Pitot tube inlet could not be successfully applied[1]. In this work, on the basis of experience, measures such as multiple regional iteration, choosing low relaxation factor in the initial stage, and giving the appropriate initial field, were taken to obtain stable and convergent results. Specifically, the method used in this work

was based on a large longitudinal disturbance (small transverse disturbance) flow potential equation. A mixed difference scheme was used. A directional derivative method was used to accurately insert the surface boundary conditions. We either started with a zero initial field or with a known solution to a similar condition, or with a solution of a one-dimensional entropy flow as the initial internal flow field to solve the difference equation by using a regional multi-layer relaxation iteration method. Finally, the precise potential flow was used to make corrections (i.e., to use the small transverse disturbance potential solution as the initial field to solve the precise velocity potential equation). This method was used to calculate the inlet described in reference [2] as well as inlets of other geometric shapes. The incident flow Mach number is $M_\infty = 0.72 \sim 1.27$. The outlet Mach number is $M_2 = 0.205 \sim 0.82$. The calculated median flow velocity, pressure coefficient distribution, and the shape and position of shock wave are in agreement with experimental results.

II. Basic Equations

When the Mach number of the incident flow is not too large (e.g., less than 1.3), the iso-entropic inviscid assumption is valid for a steady flow in an axisymmetric inlet. The velocity potential equation is:

$$\left(1 - \frac{u^2}{a^2}\right)\phi_{xx} + \left(1 - \mu\frac{v^2}{a^2}\right)\phi_{yy} - \mu\frac{2uv}{a^2}\phi_{xy} + \frac{\phi_y}{y} = 0 \qquad (1)$$

where x and y are the axial and radial direction of the cylindrical coordinate, respectively. u and v are the axial and radial components of the flow, respectively. a is the local sonic speed. ϕ_x, ϕ_y, ϕ_{xy}, ϕ_{xx} and ϕ_{yy} are the first and second order derivatives of the disturbed velocity potential function ϕ (x,y) with respect to x, y, respectively. The local sonic speed a is:

$$a = \sqrt{a_\infty^2 + \frac{\gamma-1}{2}\left[q_\infty^2 - (u^2 + \mu v^2)\right]} \qquad (2) \qquad /26$$

In equation (1), μ is a coefficient. When μ=1, equation (1) is the precise velocity potential equation. When μ=0, equation (1) becomes a large disturbance velocity potential equation in the x-axis direction.

a_∞ represents the sonic speed of the incident flow in the expression for a. q_∞ is the incident flow velocity and γ is the adiabatic index.

III. Division of Computation Region and Difference Lattice

Because the difference computation is calculated on a physical plane, the size of the region to compute will affect the convergence and stability of the results. When the incident flow is subsonic, shock waves are only formed locally near the cowl. The difference computation is relatively stable and the computed area needs not be too large. When the incident flow is supersonic, the front far field boundary only needs to include

the front of the separated bow wave. However, the side field and rear field must be sufficiently large to ensure the stability of the separated bow wave. Furthermore, it should not hinder the acceleration of the supersonic flow behind the wave in the inlet to become supersonic. In this case, the far field boundary might be selected to be around 1000R, where R is the cross-section of the inlet (see Figure 1). When the computed area is too small, it may lead to the oscillation or even divergence of the solution.

The lattice is divided orthogonally along the x and y direction. In order to make the lattice points also full on the body surface, the spacings are not equal (see Figure 2). Near the leading edge of the inlet, the meshes are closer. The mesh spacing is usually determined according to a law of algebraic series. The ratio of two neighboring lattice spacing is generally controlled at under 2. Local points may exceed this limit.
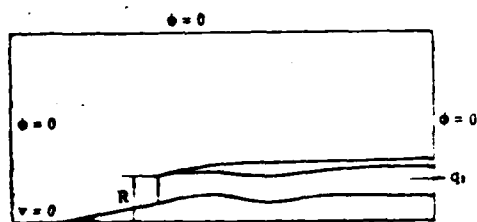
Figure 1. Computed Region and Boundary Conditions
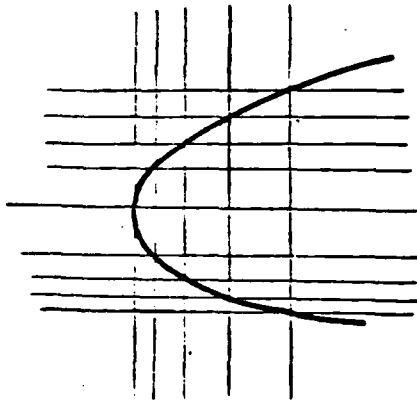
Figure 2.   Unequal Lattice Spacing

In order to reduce the computing time, a method to gradually decrease the spacing of the meshes is used. Initially, a relatively loose mesh (42x51) is used. After the flow field stabilized, the meshes are tightened (81x100) in order to obtain better flow field parameters.

IV.   Boundary Conditions

1.   Far Field Boundary Condition. The disturbed velocity potential in the ar front field, side far field, and rear far field outside the inlet is given to be $\phi=0$.

The given flow velocity in the field far away from the outlet is q_2.

2. Centerline Boundary Condition. Because of axisymmetry, $v=\phi_y=0$ at the centerline.

3. Centercone Leading-edge Boundary Condition. The stationary point condition is used for all points on the leading-edge of the centercone, i.e., $u=\phi_x + q_\infty=0$, $v=0$.

4. There are two ways to treat the boundary conditions for the leading-edge of the cowl.

(1) $u=\phi_x+q_\infty=0$, based on a blunt leading-edge.

(2) Based on a sharp leading-edge, the point is split into two. The upper point is located on the upper surface and is treated as a body boundary point of the upper surface. It is considered as an extension of the upper surface in the computation. Furthermore, the ϕ value on the extended surface is ext apolated. The lower point is located on the lower surface and is treated as a body surface boundary point of the lower surface. In the computation, it is assumed to be an extension of the lower surface. Furthermore, the ϕ value on the extended surface is extrapolated.

5. Body Surface Boundary Conditions. Let us assume that the equation of the body surface is $y=f(x)$. A directional derivative method is used to accurately meet the body surface boundary condition, i.e.,

$$\phi_y=f'(x) \ (q_\infty+\phi_x) \tag{3}$$

If s is used to express the direction along the body surface, the directional derivative equation can be written as

$$\phi_s =\phi_x \cos(x,s) + \phi_s \cos(y,s) \tag{4}$$

21

where

$$\cos(x, s) = \frac{1}{\sqrt{1 - f'(x)^2}}$$

$$\cos(y, s) = \frac{f'(x)}{\sqrt{1 - f'(x)^2}} \tag{4}$$

By summarizing the above, we get

$$\tag{5}$$

$$\phi_x = \frac{\phi_s}{\sqrt{1 - f'(x)^2}} - q_\infty \frac{f'(x)^2}{1 - f'(x)^2}$$

$$\phi_y = (q_\infty - \phi_x) f'(x) \tag{6}$$

The second order derivative of the perturbed velocity potential on the body surface can also be expressed in terms of directional derivatives:

$$\tag{7}$$

$$\phi_{xs} = \phi_{ys} \sqrt{1 - f'(x)^2} - \phi_{ss} f'(x)$$

$$\phi_{xx} = [\phi_{xs} - \phi_{ys} f'(x)] \sqrt{1 - f'(x)^2} - \phi_{ss} f'(x)^2 \tag{8}$$

where the second derivative ϕ_{yy} is expressed as the following using an analytical extension method:

$$\phi_{yy} = \frac{2}{\Delta y_j} \left(\frac{\phi_{i,j+1} - \phi_{i,j}}{\Delta y_j} - \phi_y \right) \qquad \text{(for upper surface)} \tag{9}$$

OR

$$\phi_{yy} = \frac{1}{\Delta y_{j-1}} \left(\phi_y - \frac{\phi_{i,j} - \phi_{i,j-1}}{\Delta y_{j-1}} \right) \qquad \text{(for lower surface)} \tag{10}$$

Here, the subscripts i and j represent the lattice numbers of body surface points.

In these equations, the formulas to calculate the partial derivatives ϕ_s, ϕ_{xs}, and ϕ_{ys} of perturbation velocity potential

22

in the direction tangent to the body surface are as follows
(using the positive slope surface as an example)

$$\phi_s = \frac{\phi_{i+1,j+1}\,\Delta s_{i-1}^2 + \phi_{i,j}(\Delta s_i^2 - \Delta s_{i-1}^2) - \phi_{i-1,j-1}\,\Delta s_i^2}{\Delta s_i \Delta s_{i-1}(\Delta s_i - \Delta s_{i-1})} \qquad (11)$$

$$\phi_{ss} = \frac{(\phi_s)_{i+1,j+1} - (\phi_s)_{i-1,j-1}}{\Delta s_i - \Delta s_{i-1}} \qquad (12)$$

$$\phi_{ys} = \frac{(\phi_y)_{i+1,j+1} - (\phi_y)_{i-1,j-1}}{\Delta s_i - \Delta s_{i-1}} \qquad (13)$$

$$(14) \qquad /28$$

$$\phi_s = \frac{\phi_{i,j}[(\Delta s_{i-1} + \Delta s_{i-2})^2 - \Delta s_{i-1}^2] - \phi_{i-1,j-1}(\Delta s_{i-1} + \Delta s_{i-2})^2 + \phi_{i-2,j-2}\,\Delta s_{i-1}^2}{\Delta s_{i-1}\Delta s_{i-2}(\Delta s_{i-1} + \Delta s_{i-2})}$$

$$\phi_{ss} = \frac{(\phi_s)_{i,j} - (\phi_s)_{i-1,j-1}}{\Delta s_{i-1}} \qquad (15)$$

$$\phi_{ys} = \frac{(\phi_y)_{i,j} - (\phi_y)_{i-1,j-1}}{\Delta s_{i-1}} \qquad (16)$$

$$\Delta s_i = \sqrt{\Delta x_i^2 + \Delta y_i^2} \qquad (17)$$

where

$$\Delta s_{i-1} = \sqrt{\Delta x_{i-1}^2 + \Delta y_{i-1}^2} \qquad (18)$$

$$\Delta s_{i-2} = \sqrt{\Delta x_{i-2}^2 + \Delta y_{i-2}^2} \qquad (19)$$

Equations (11), (12) and (13) are for subsonic points, and (14),
(15) and (16) are for supersonic points.

V. The Mixed Difference Scheme

Different difference schemes for x-direction partial
derivatives are used for supersonic and subsonic points in the
flow field. For a supersonic point, the difference of the

23

x-direction partial derivative employs a downwind scheme. For a
subsonic point, a center scheme is used. The y-direction partial
derivatives employ the center difference scheme. With the
exception of some special cases, a second order accuracy scheme
is used for all first derivatives and a first order accuracy
scheme is used for all second derivatives in order to match the
scheme to the accuracy desired. The main formulas are:

$$\phi_x = \frac{\phi_{i,j}[(\Delta x_{i-1} + \Delta x_{i-1})^2 - \Delta x^2_{i-1}] - \phi_{i-1,j}(\Delta x_{i-1} + \Delta x_{i-2})^2 + \phi_{i-2,j}\Delta x^2_{i-1}}{\Delta x_{i-2}\Delta x_{i-1}(\Delta x_{i-1} + \Delta x_{i-2})} \tag{20}$$

$$\phi_{xx} = 2\frac{\phi_{i,j}\Delta x_{i-2} - \phi_{i-1,j}(\Delta x_{i-1} + \Delta x_{i-2}) + \phi_{i-2,j}\Delta x_{i-1}}{\Delta x_{i-2}\Delta x_{i-1}(\Delta x_{i-2} + \Delta x_{i-1})} \tag{21}$$

$$\phi_{xy} = \frac{1}{(\Delta y_j + \Delta y_{j-1})(\Delta x_{i-1} + \Delta x_{i-2})\Delta x_{i-1}\Delta x_{i-2}} \tag{22}$$
$$\times \{(\phi_{i,j+1} - \phi_{i,j-1})[(\Delta x_{i-1} + \Delta x_{i-2})^2 - \Delta x^2_{i-1}]$$
$$- (\phi_{i-1,j+1} - \phi_{i-1,j-1})(\Delta x_{i-1} + \Delta x_{i-2})^2$$
$$+ (\phi_{i-2,j+1} - \phi_{i-2,j-1})\Delta x^2_{i-1}\}$$

$$\phi_x = \frac{\phi_{i+1,j}\Delta x^2_{i-1} + \phi_{i,j}(\Delta x^2_i - \Delta x^2_{i-1}) - \phi_{i-1,j}\Delta x^2_i}{\Delta x_{i-1}\Delta x_i(\Delta x_{i-1} + \Delta x_i)} \tag{23}$$

$$\phi_{xx} = 2\frac{\phi_{i+1,j}\Delta x_{i-1} - \phi_{i,j}(\Delta x_{i-1} + \Delta x_i) + \phi_{i-1,j}\Delta x_i}{\Delta x_{i-1}\Delta x_i(\Delta x_{i-1} + \Delta x_i)} \tag{24}$$

$$\phi_{xy} = \frac{1}{(\Delta y_j + \Delta y_{j-1})(\Delta x_{i-1} + \Delta x_i)\Delta x_{i-1}\Delta x_i} \tag{25}$$
$$\times [(\phi_{i+1,j+1} - \phi_{i+1,j-1})\Delta x^2_{i-1} + (\phi_{i,j+1} - \phi_{i,j-1})$$
$$\times (\Delta x^2_i - \Delta x^2_{i-1}) - (\phi_{i-1,j+1} - \phi_{i-1,j-1})\Delta x^2_i]$$

$$\phi_y = \frac{\phi_{i,j+1}\Delta y^2_{j-1} + \phi_{i,j}(\Delta y^2_j - \Delta y^2_{j-1}) - \phi_{i,j-1}\Delta y^2_j}{\Delta y_j\Delta y_{j-1}(\Delta y_j + \Delta y_{j-1})} \tag{26}$$
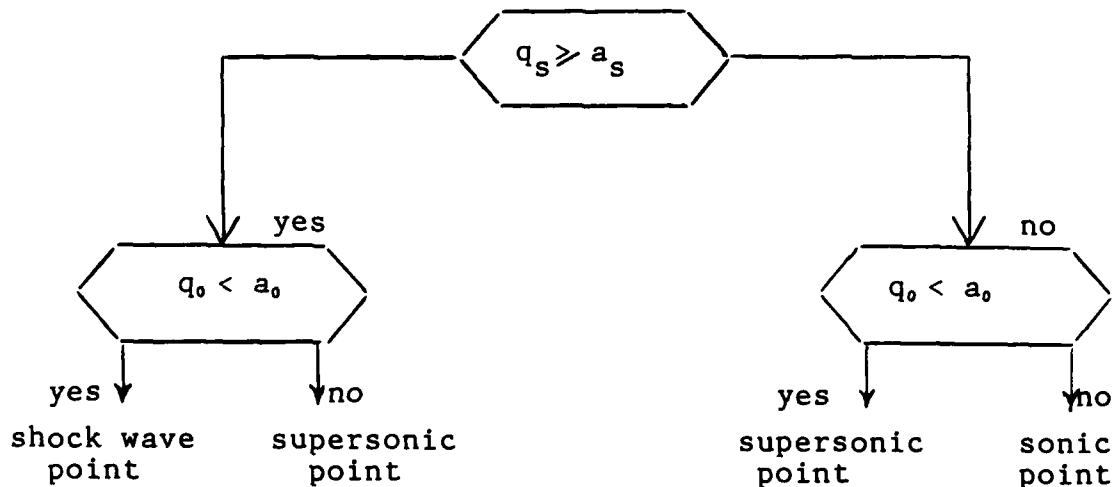
$$\phi_{yy} = 2\frac{\phi_{i,j+1}\Delta y_{j-1} - \phi_{i,j}(\Delta y_{j-1} + \Delta y_j) + \phi_{i,j-1}\Delta y_j}{\Delta y_{j-1}\Delta y_j(\Delta y_{j-1} + \Delta y_j)} \tag{27}$$

24

where equations (20), (21) and (22) are in the downwind mode and
(23)-(27) are in the center mode.

VI. Velocity Determination and Treatment of Shock Wave and Sonic
Speed Points

In establishing the difference equation for a point in the flow field,
it is necessary to determine the velocity at that point to
see whether it is subsonic or supersonic in order to employ
a comparable difference scheme in iteration. The determination
process is shown as follows:

```
                        ┌─────────────────┐
                    ┌───┤   q_s ≥ a_s     ├───┐
                    │   └─────────────────┘   │
                    ▼                         ▼
                  yes                        no
          ┌─────────────────┐      ┌─────────────────┐
          │   q_0 < a_0      │      │   q_0 < a_0      │
          └───────┬─────┬────┘      └───────┬─────┬───┘
           yes ▼       ▼ no          yes ▼       ▼ no
        shock wave  supersonic    supersonic   sonic
          point      point          point      point
```

where the subscript s indicates that a one-sided formula is used
and the subscript 0 indicates that the center formula is used.

Sonic and shock wave points are treated as subsonic points. For a sonic point, notice that equation (1) becomes

$$\phi_{yy} + \phi_y/y = 0 \tag{28}$$

VII. Multi-regional Multi-layer Linear Relaxation Iteration Method

If the control function (1) is written as

$$R_1\phi_{xx} + R_2\phi_{yy} + R_3\phi_{xy} + R_4\phi_y = 0 \tag{29}$$

We get the following by substituting equations (20)-(27) into (29).

$$A\phi_{i,j-1} + B\phi_{i,j} + C\phi_{i,j+1} = D \tag{30}$$

If equation (30) is written for every point on all vertical lattice lines (i=constant) and the coefficients A, B, C and D are known, then a series of tridiagonal equations is the result. Hence, it is possible to solve this problem by a chasing method.

In a center-body conical inlet, the internal is mostly a contracting-expanding conduit. With a supersonic incident flow, when the computation begins with a zero initial field, it is equivalent to calculating the flow field from a supersonic flow field. In this case, the wall disturbance in the expanding tube will lead to the further acceleration of the flow. Thus, calculated results will further deviate from the actual flow. However, the boundary condition at the outlet requires the presence of subsonic flow in the expanding channel. For this reason, when the entire field is linearly relaxed along the y-direction, the wall disturbance inside the tube and the disturbance of the reverse pressure at the exit are seriously out

26

of coordination. In response to this special characteristic, wall disturbance must be suppressed in the initial stage of the calculation in order to accelerate the propagation of the inverse pressure. However, because the center-body blocked the disturbance of inverse pressure propagating along the x-direction relaxation line, when we used the alternate direction linear relaxation iteration method to calculate the experimental data, it did not converge over long iterations. For this reason, a regional multi-layer lower order relaxation iteration method was used in this work, i.e., the entire flow field was linearly relaxed in the y-direction. In addition, lower relaxation was used in the initial stage. The entire flow field was divided into internal and external flow areas. Or, the internal flow could be further divided into a contracting section, an expanding section and a straight-section. Moreover, the number of relaxation iterations for the internal flow might be increased (e.g., one iteration for external flow, 1-5 iterations for internal flow and 1-5 times more iterations for the expanding section). Until the flow field is essentially stable, then the entire flow field was treated as a whole by relaxation iteration. Our experience indicates that this method not only can ensure the /30 stability of the computation but also can accelerate convergence. This is because it not only facilitates the propagation of the inverse pressure disturbance at the outlet but also can adjust the coordination between wall disturbance and outlet pressure disturbance. Consequently, an initial flow field, similar to the actual flow field can be established. This facilitates the

27

solution of a flow field starting from a zero initial field
because its structure is not known.

Conventional or improved iterations may be used in the
linear relaxation iteration method. The improved iteration not
only can speed up the rate of convergence but also will not cause
a supersonic flow field to become divergent. Different
relaxation factors were used in the supersonic and subsonic
regions. A relaxation factor ω is defined as follows:

$$\phi_{i,j}^{(n)} = \phi_{i,j}^{(n-1)} + \omega \left(\phi_{i,j}^{*(n)} - \phi_{i,j}^{(n-1)} \right)$$

where the superscript (n) represents the number of iterations and
$\phi_{i,j}^{*(n)}$ represents the result of nth iteration not yet treated by
relaxation.

VII. Initial Field and Convergence Standard

The selection of the initial field is very important. It
will directly affect the convergence and time of computation. It
is feasible to use a zero initial field (i.e., the disturbance
velocity potential $\phi=0$) for the external flow of the inlet due to
the fact that it is relatively simple. It also makes the
computation relatively more stable. However, for the internal
flow field of the inlet, if a one-dimensional flow method can be
used to estimate an initial flow field, then the rate of
convergence can be increased. If this is difficult to
accomplish, then we can also start from a zero initial field. In
this case, because the initial field is far different from the

28

final solution, relatively smaller relaxation factors must be used over a longer period of time to perform iterations in layers during the initial stage of computation to prevent it from becoming divergent.

Whether an iteration is convergent must be evaluated by the computing process. Let us assume that the following is true for all points

$$\left|\frac{\phi_{i,j}^{(n)}-\phi_{i,j}^{(n-1)}}{\phi_{i,j}^{(n)}}\right|_{max} = \Delta\bar{\phi}^{(n)}$$

Then, the standard convergence can be specified as:

$$\Delta\bar{\phi}^{(n)} \leqslant 10^{-3} \sim 10^{-5}$$

In this work, in addition to the above convergence standard, the main standard of convergence used is that the relative error of any cross-sectional flow rate is less than ε ($\varepsilon=0.01\sim0.05$):

$$\Delta\psi^{(n)}/\psi_e \leqslant \varepsilon$$

where $\Delta\phi^{(n)}=|\phi_i^{(n)}- \phi_e^{(n-1)}|_{max}$, ϕ_i is the gas flow rate across the ith cross-section and ϕ_e is the flow rate across the exit cross-section. Our experience shows that it is a convergence criterion which reflects the physical nature of the flow. It not only can avoid a false convergence due to using excessively small relaxation factors but also can prevent any misjudgement caused by velocity potential fluctuation due to the pressure of sonic line or small shock wave vibration when the incident flow is near sonic or supersonic.

29

IX. Examples

The method introduced above was used to calculate the following flow conditions of the inlet with a conical centerbody.

(1) M_∞=1.2278,	M_2=0.3481	(E)
(2) M_∞=1.2278,	M_2=0.2489	/31
(3) M_∞=1.2278,	M_2=0.2053	
(4) M_∞=1.0453,	M_2=0.3435	(A)
(5) M_∞=1.0453,	M_2=0.3025	
(6) M_∞=1.0453,	M_2=0.2056	

In addition, we also calculated internal and external transonic flow field of the first type (60-40) inlet reported in reference [2].

The computation was carried out on a SIEMENS 7760 computer using two sets of lattices, i.e., 42x51 and 81x100. The criterion of convergence used is $(\Delta\psi/\psi_e)<1-3\%$. The numbers of iterations required to obtain a convergent solution are approximately 320 and 360, respectively, taking about 500 and 800 seconds of CPU time. For the first type of inlet reported in reference [2], we get the following solutions:

Small transverse disturbance (μ=0) solutions with 42x51 and 81x100 meshes, as well as the accurate velocity potential solution (μ=1) with 42x51 meshes when the incident flow Mach number M_∞=1.27 and the flow coefficient CA=0.655.

Small transverse disturbance solution with 42x51 meshes when M_∞=1.27 and CA=0.721.

Small transverse disturbance solution with 42x51 meshes when M_∞=1.27 and CA=0.762.

Comparisons of major results to experimental data[2] are
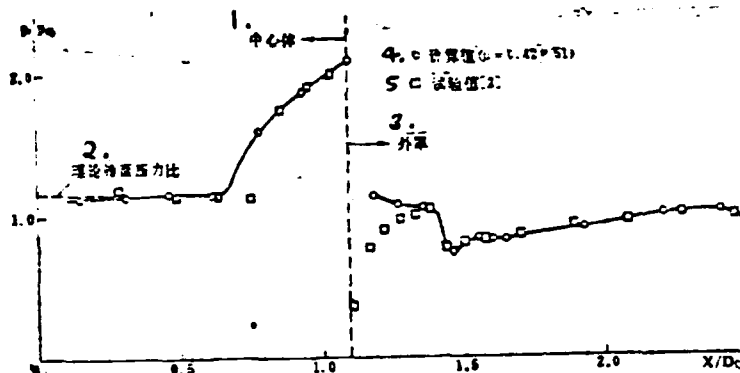shown in Figures 3~8. They show that:

Figure 3.   Pressure Distribution Along Centerbody and Cowl
            Surface (M_∞=1.27, M_∞=0.5413, CA=0.655)

            1.   centerbody
            2.   theoretical cone surface pressure ratio
            3.   cowl
            4.   calculated value (μ=0, 42x51)
            5.   experimental value reported in reference [2]

Figure 4.   Pressure Distribution Along Centerbody and Cowl
            Surface (M_∞=1.27, M_∞=0.6329   CA=0.721)

            1.   centerbody
            2.   theoretical cone surface pressure ratio

31

3. cowl
4. calculated value ($\mu=0$, 42x51)
5. experimental data reported in reference [2]

Figure 5. Pressure Distribution Along Centerbody and Cowl /32
Surface ($M_\infty=1.27$, $M_\infty=0.7058$, CA=0.762)

1. centerbody
2. theoretical cone surface pressure ratio
3. cowl
4. calculated value ($\mu=0$, 42x51)
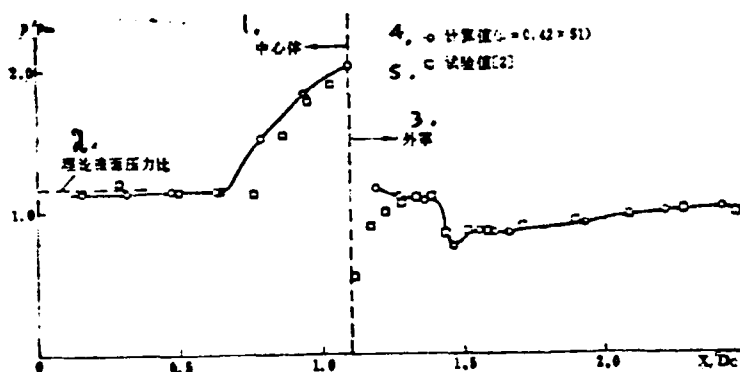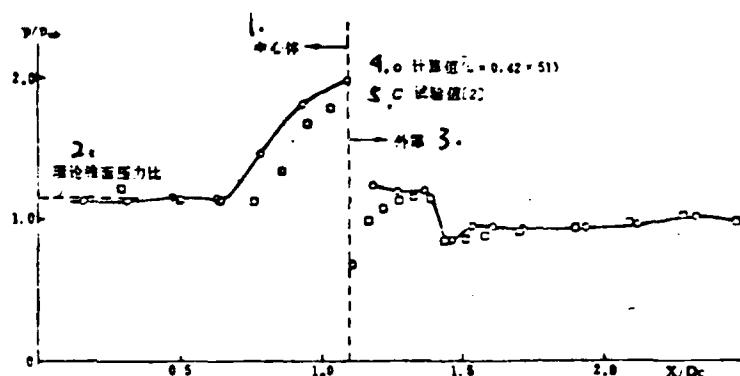5. experimental value reported in reference [2]
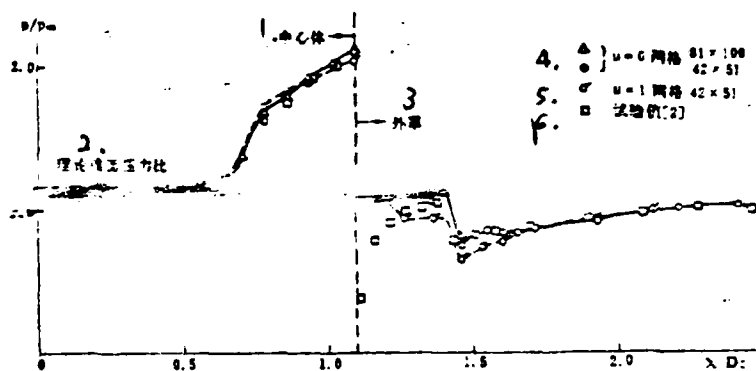

Figure 6. Comparison of Pressure Distribution Along Centerbody
and Cowl Surface ($M_\infty=1.27$, $M_\infty=0.5413$, CA=0.655)

1. centerbody
2. theoretical cone surface pressure ratio

3. cowl
4. $\left.\begin{matrix}\Delta \\ o\end{matrix}\right\} \mu=0$ $\begin{matrix}81\times100 \\ 42\times51\end{matrix}$ meshes
5. σ $\mu=1$, 42x51 meshes
6. experimental data reported in reference [2]

1. For a supersonic inlet, when the center conical angle and cowl leading edge angle are not too large, the results obtained by using a mixed difference method (such as pressure distribution on surface and position and shape of the bow-shaped shock wave) with a small transverse disturbance steady transonic velocity potential agree well with the experimental data (See Figures 3~5 where D_c is the diameter of the cross-section of the entrance of the inlet). The accuracy is already acceptable for engineering applications when using the 42x51 mesh size. There is no need to make corrections by tightening the meshes or using the full velocity potential equation (See Figure 6).

2. Figure 7 shows that the position of the shock wave is determined from the pressure distribution curves (Figures 3-5) based on the pressure ratio. The calculated value is 1.405. When the experimental data was processed, it was chosen to be 1.383 by taking loss into account[2]. The position of shock wave obtained by this method is located one mesh ahead of the experimental result. This is due to the use of a non-conservative difference scheme (see references [3] and [4]).

3. Near the leading-edge of the cowl, the calculated pressure is higher than the experimental value. It is so even with the solution to the accurate velocity potential. This is so even with the solution partially separated near the leading edge

33

under these three conditions. The total pressure loss is
significant. Assumptions such as inviscidy and isoentropy are no
longer valid. However, the separated area is very small and will
not affect the pressure drag of the entire inlet. The
engineering value of this method will not be hurt.

4. The calculated intensity of the conical shock wave and
the cone Mach number (pressure) are in good agreement with
theoretical[5] and experimental results (see Figures 3,4,5 and
8). Because the meshes are loose, the position of the shock wave
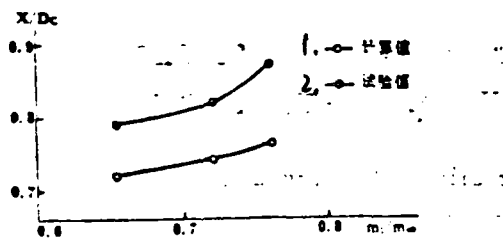cannot be easily determined. However, the error is less than one
mesh space.

Figure 7. Distance Between Shock Wave and Cone Tip vs. Flow Rate   /33
        (M_∞=1.27)

        1. calculated value
        2. experimental value

34
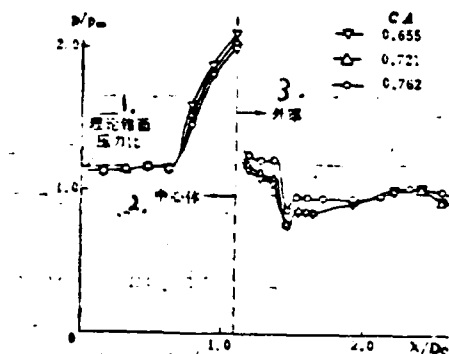
Figure 8. Pressure Distribution Along Centerbody and Cowl vs.
Flow Rate

    1.   theoretical cone surface pressure ratio
    2.   centerbody
    3.   cowl

X. Conclusions

1. In this work, we successfully calculated the internal
and external flow fields of a supersonic inlet based on the large
disturbance axial velocity potential equation by using a simple
non-rotational mixed difference scheme, accurate surface boundary
conditions and the regional linear relaxation iteration
technique. This method has good convergence and stability. The
accuracy and required computer time can meet practical
engineering needs.

2. When calculating the flow field of an inlet with
complicated geometry, conventional linear relaxation iteration
techniques cannot easily render convergent solutions because the

flow parameters in various regions are not in coordination. This problem can be overcome by using multi-layer iteration and using a low relaxation factor in the initial stage or by choosing an initial field closer to the real solution. The experience gained in this work can prepare us to extend our work to calculate the internal and external flow fields of complicated three-dimensional inlets.

References

[1] Luo Shijun et al, Computation of Axisymmetric Transonic Inlet, Journal of Aerodynamics, 4 (1982).

[2] Woollett. R.R., Meleason, E.T. and Choby, D.A., Transonic Off-Design Drag and Performance of Three Mixed-Compression Axisymmetric Inlets, NASA TM X-3215, 1975.

[3] Arlinger, B.G., Axisymmetric Inlets Flow at Low Supersonic Mach Numbers, Symposium Transsonicum II, pp. 201-207, 1975.

[4] Rizzi, A.W. and Schmidt, W., Study of Pitot-Type Supersonic Inlet-Flow Field Using the Finite-Volume Approach, AIAA Paper No. 78-1115, 1978.

[5] Dailey, C.L. and Wood, F.C., Computation Curves for Compressible Fluid Problems. New York, John Wiley, Sons, Inc. 1949.

A MIXED FINITE DIFFERENCE ANALYSIS OF THE INTERNAL AND EXTERNAL TRANSONIC FLOW FIELDS OF INLETS WITH CENTERBODY

Luo Shijun   Shen Huili   Ji Minggang

Xing Zongwen

(Northwestern Polytechnical University)

Dong Songye   Han Aiqing

(31 th Institute, the Ministry of Astronautics Industry)

Abstract

, A mixed finite difference method for calculating the external and internal flow field around inlet with centerbody is presented. First, calculation by mixed finite difference method of the velocity potential equation with small disturbance in the transverse direction using cartesian mesh, irrotational schemes and exact body surface boundary conditions is carried out to obtain a basic field solution including the shape and location of the shock and the sonic line. Then, the full potential equation is used to improve the accuracy of the computed value of field variables. The use of multi-layer line relaxations along the radial lines is effective for inlet with centerbody, and in this case, more relaxation sweeps are carried out (with smaller relaxation factor) inside the inlet than the relaxation sweeps carried out outside the inlet. Computations have been made for axisymmetric inlet with different freestream Mach numbers $M_\infty = 1.04 \sim 1.27$. Computation results show that the method is promising.

Numerical Method for Viscous Shock-layer Near The Stagnation Line of a Blunt Body

Yu Qingwen and Wang Ruquan

(The Computer Center, Academia Sinica)

I. Introduction

When studying a hypersonic viscous flow around a blunt object, the prediction of aerodynamic and thermodynamic parameters in the stagnation region is also very important. When the viscous layer is very thin, the classical boundary layer equation is always used. When the mutual interference between a viscous gas and an inviscid flow is considered, the boundary layer model is no longer applicable. The viscous shock-layer equation can be used in the flow field of a wide range of incident Mach number and Reynolds number[1,2].

In recent years, many people have dedicated their effort on the computation of the flow field near the stagnation line.[3,4,5] Scme of them crossed the shock wave and some separated the shock wave. However, when the shock wave was separated, they neglected the effect of the downstream flow field on the stagnation region, which usually resulted in large error. Because the flow near the stagnation line is in the subsonic range in the shock layer, the physical equations describing the flow characteristics are essentially elliptical. Hence, when the effect of the downstream flow on the stagnation line is considered, it very often leads to new unknown parameters in the equations. Thus, there are more

unknowns than equations to make the problem non-unique. Just for this reason, many people discarded parameters relevant to the downstream flow in their studies.

In this work, based on the viscous shock layer equation, a set of second order normal differential equations near the stagnation line is derived. In order to reflect the effect of downstream flow on the stagnation point, the shock wave boundary condition is expanded into a Taylor series around the stagnation point, including an unknown parameter $e_2 = (1/2) \cdot (d^2 \Sigma / dx^2)$. It is related to the curvature of the segmental shock wave near the stagnation point which remains unknown unless the flow field at the head is solved. We used the curvature of an ideal shock wave to approximate it and the numerical results agree with the overall solution.

II. Basic Equations

The basic equations describing the flow characteristics near the stagnation point are the viscous shock layer equations[1]. Near the stagnation point, the solution can be expanded into the following[6]:

$$u = u_1(y)x \qquad (2.1)$$

$$v = -(1 - \tfrac{1}{2}k^2 x^2)v_0(y) \qquad (2.2)$$

$$p = (1 - k^2 x^2)p_0(y) - \tfrac{1}{2}x^2 p_2(y) \qquad (2.3)$$

$$T = (1 - k^2 x^2) T_0(y) \qquad (2.4)$$

$$\rho = \rho_0(y) \qquad\qquad (2.5) \qquad /36$$

$$\mu = \mu_0(y) \qquad\qquad (2.6)$$

$$\lambda = \lambda_0(y) \qquad\qquad (2.7)$$

$$\varepsilon = \varepsilon_0 + \varepsilon_2 x^2 + \dots \dots \qquad (2.8)$$

The last equation is the expansion of the distance of shock wave separation at the stagnation point. A series of normal differential equations cna be obtained by substituting the above equations into the viscous shock layer equation. After using factors such as R, V_∞, ρ_∞, W_∞, λ_∞, μ_∞, $p_\infty V_\infty^2$, $W_\infty V_\infty^2/R$, and R/W_∞ to render length, velocity, density, mean molecular weight, thermal conductivity, viscosity, pressure, temperature and isobaric specific heat non-dimensional, the viscous shock layer equation in the stagnation region is as follows:

$$\frac{1}{Re}\frac{d}{dy}\left(\mu_0\frac{du_1}{dy}\right) + \left(\rho_c v_0 - \frac{\pi_c \mu_c}{Re}\right)\frac{du_1}{dy} + \left[\frac{(k\rho_c v_c - \rho_c u_1)}{H}\right. \qquad (2.9)$$
$$\left. - \frac{k}{Re}\frac{d}{dy}\left(\frac{\mu_0}{H}\right)\right] u_1 + \frac{(2k' p_0 + p_1)}{H} = 0$$

$$- \quad \delta\frac{d}{dy}\left(\mu_0\frac{dT_0}{dy}\right) + (\delta\pi_0 \mu_0 + C, \rho_c v_0)\frac{dT_c}{dy} - v_0\frac{dv_0}{dy} = 0 \qquad (2.10)$$

$$\frac{d(\rho_c v_0)}{dy} + \pi_c \rho_c v_0 - \frac{2\rho_c u_1}{H} = 0 \qquad\qquad (2.11)$$

$$\frac{dp_0}{dy} - l_1 \rho_c v_0 \frac{dv_0}{dy} = 0 \qquad\qquad (2.12)$$

$$\frac{dp_1}{dy} + \frac{2k\rho_c u_1}{H}(l_1 u_1 - l_1 k v_0) = 0 \qquad\qquad (2.13)$$

$$p_c = \rho_c T_0 \qquad\qquad (2.14)$$

$$\mu_c = \mu_0(T) \qquad\qquad (2.15)$$

where H=1+ky, $\pi_0 = 2k/(1+ky)$, $\delta = C_p/RePr$, and (l_1, l_2) are control parameters. (0,1) is the thin shock layer equation, (0,0) is the

39

boundary layer equation and (1,1) is the viscous shock layer equation.

In a chemical equilibrium, it is necessary to change the equations of energy and state. In this case, C_p and W are not constants. Instead, they are functions of p and T. We employed an approximate thermodynamic function table method to calculate. When the gas is in equilibrium, the equations of energy and state are as follows:

$$\delta \frac{d}{dy}\left(\mu_0 \frac{dT_0}{dy}\right) + (h_T \rho_0 v_0 + \pi_0 \delta \mu_0)\frac{dT_0}{dy} - (1 - \rho_0 h_p)v_0 \frac{dp_0}{dy} = 0 \qquad (2.16)$$

$$p_0 = \rho_0 T_0 / W_0 \qquad (2.17)$$

where h_T and h_p represent the derivatives of enthalpy with respect to temperature and pressure. In summary, the stagnation line equation is a set of quasi-linear differential equations with u_1, v_0, p_0, p_2, T_0, ρ_0 and μ_0 as unknowns.

III. Boundary Conditions

Let us assume the following conditions exist on the body surface:

$$u_1 = 0 \qquad (3.1)$$
$$v_0 = 0 \qquad (3.2) \qquad /37$$
$$T_0 = T_W \qquad (3.3)$$

The shock wave is considered as an interrupted surface and the classical Rankine-Hugoniet condition is the external boundary condition. It is expanded into a Taylor series at the stagnation point. By using equation (2.8), the expressions on the shock

40

wave can be obtained as follows:

$$u_{1e} = k - \frac{2}{\gamma - 1}\left(1 - \frac{1}{M_\infty^2}\right)\frac{2e_1}{1 + ke_0} \tag{3.4}$$

$$v_{0e} = \frac{\gamma - 1}{\gamma + 1} + \frac{2}{(\gamma + 1)M_\infty^2} \tag{3.5}$$

$$\rho_{0e} = \left(\frac{\gamma - 1}{\gamma + 1} + \frac{2}{\gamma(\gamma + 1)M_\infty^2}\right)^{-1} \tag{3.6}$$

$$p_{1e} = \frac{2}{\gamma + 1}\left[\frac{8e_1}{1 + ke_0}\left(\frac{e_1}{1 + ke_0} - k\right) + \frac{\gamma - 1}{\gamma M_\infty^2}k^2\right] \tag{3.7}$$

$$p_{0e} = \frac{2}{\gamma + 1} - \frac{\gamma - 1}{\gamma(\gamma + 1)M_\infty^2} \tag{3.8}$$

The unknown parameter ϵ_2 appears in equations (3.4) and (3.7). Therefore, the boundary value problem of the differential equation is not unique. ϵ_2 is dependent upon the downstream flow field. In reality, it cannot be predicted and will require repeated iterations to be accurately determined[10]. Our objective is to independentally solve the stagnation point equation. In practice it was found that it is successful to use the inviscid shock wave to approximate ϵ_2. It is not too different from the stagnation point solution obtained by using a linear method[12]. For convenience, a small amount of data can be used to prepare an $\epsilon_2 \sim M_\infty$ curve (See Figure 2).

In equilibrium, because the temperature T is hidden in the equations, the shock wave equation must be determined by iteration.
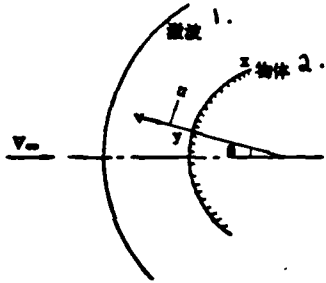
Figure 1.   The Coordinate System

        1.   shock wave
        2.   body

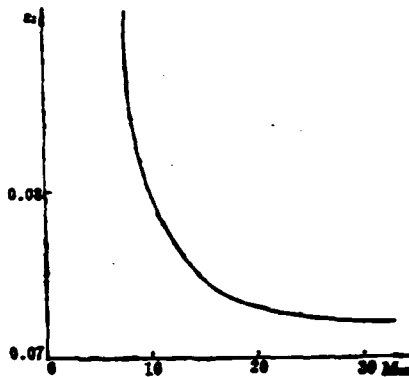Figure 2. $\epsilon_2 \sim M_\infty$ Curve

IV.   Numerical Method

Because some physical quantities have larger gradients near the body surface, after considering the stability of the numerical method and the accuracy of the results, we used a certain coordinate transformation to automatically tighten the lattice at places where the gradient is large.   In this work, we used the following equation

$$f=\ln(1+Gy)/\ln(1+G) \qquad (4.1)$$

where G is the lattice control parameter. When the Reynolds
number Re_∞ is large, G is chosen to be larger. When Re_∞ is
small, G is chosen to be smaller depending on the accuracy
required.

We used a finite difference method to solve the boundary
value problem of the normal differential equation set. Center
difference was used for internal points to ensure that the
interrupt error is of the second order. The second order
equation is solved by a chasing method. The continuity equation
is integrated from the body surface to the shock wave. The
equations for p_0 and p_2 are integrated from the shock wave toward
the body surface. The shock wave distance can be determined by
two methods: one is to the Newtonian Method to solve non-linear
equations and the other is to use the integral of the continuity
equation. Numerical calculations show that the latter is better
than the former. The latter can improve the rate of convergence.
The formula to determine the shock wave using the Newtonian
method is

$$\varepsilon'^{(k+1)} = \varepsilon'^{(k)} - \omega \frac{\rho_t v_\bullet}{\frac{\partial(\rho_t v_c)}{\partial \varepsilon^{(k)}}} \qquad (4.2)$$

where ω is the relaxation factor ($0 \leqslant \omega \leqslant 1$). The formula based on
integrating the continuity equation is

$$\varepsilon = (\rho_t v_c)_t \Big/ \int_\bullet^1 F \, d\varsigma \qquad (4.3)$$

43

where $\qquad F = 2\rho_0/(u_1-Kv_0)/(1+f')$ $\qquad$ (A)

In gas equilibrium, we used a triple sampling function to approximate the thermodynamic function table[7,8,9]. We divided p from 100~1000 atm into one section and other pressure as another section. We used 8x17 and 22x37 to approximate the table value. The maximum relative error is less than 1%.

V. Results and Analysis

We calculated over a wide range of M_∞ and Re_∞ and compared the results to those in the literature. In Figure 3, we compared the calculated u_1 and v_0 with those obtained using a linear method[11]. The computation was carried out for $M_\infty=20$, $Re_\infty=173$, 1730, 17300, 173000, and 1730000; $\gamma=1.4$; $T_\infty=300°K$; $Pr=0.72$; $\mu=K$ $\sqrt{T}(1+S/T)$.
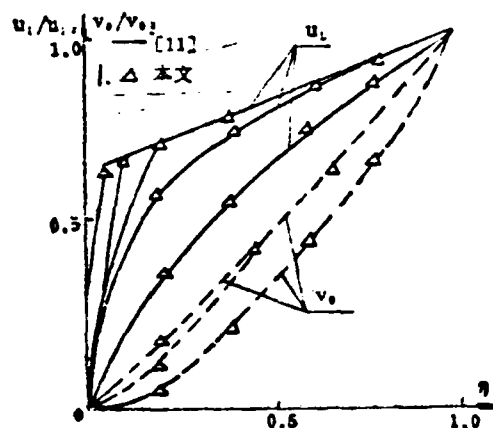

Figure 3.   The u_0 , v_1 Cross-section
$\qquad$ 1.   this work

It is obvious that the stagnation point solution obtained by using the ϵ_2 value of an inviscid flow to approximate that of a viscous flow is very similar to the solution obtained by using a linear method. For a quantitative comparison, Table 1 lists the results of this work and the data reported in reference [13].

From Table 1 we can see that the maximum error occurs in u_1. However, the relative error is less than 0.5%. If the effect of downstream flow on the stagnation region is not considered (i.e. $\epsilon_2 \equiv 0$), then the maximum error in the shock layer may reach 20%. Figure 4 shows the variation of u_1 with $\epsilon_2 = 0$ and $\epsilon_2 \neq 0$.

Figures 5 and 6 are the results obtained in equilibrium. They are also compared to the viscous equilibrium gas results obtained using a linear method and that of an ideal gas. The agreement is very good.

Table 1 Stagnation Data Obtained in this Work and by Linear

Method

变量 方法	p_0		u_1		v_0		T_0	
	3.本 文	4.直 线 法	5.本 文	6.直 线 法	7.本 文	8.直 线 法	9.本 文	10.直 线 法
0.0	0.9214	0.9212	0	0	0	0	0.014	0.014
0.2	0.9179	0.9177	0.6323	0.6321	0.0298	0.0299	0.1346	0.1349
0.4	0.9076	0.9074	0.7128	0.7098	0.0639	0.0640	0.1438	0.1439
0.6	0.8908	0.8099	0.7740	0.7705	0.0970	0.0969	0.1432	0.1433
0.8	0.8665	0.8665	0.8342	0.8328	0.1317	0.1315	0.1421	0.1421
1.0	0.8330	0.8330	0.8932	0.8964	0.1686	0.1686	0.1406	0.1406

1. parameter
2. method
3. this work
4. linear method
5. this work
6. linear method
7. this work
8. linear method
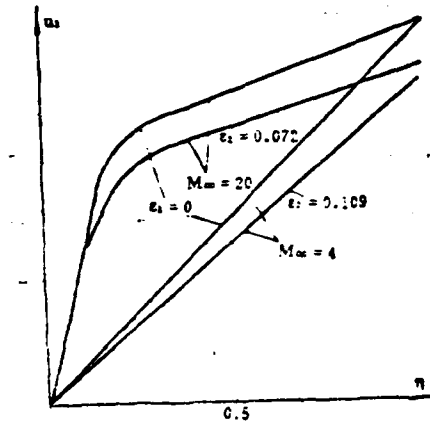9. this work
10. linear method

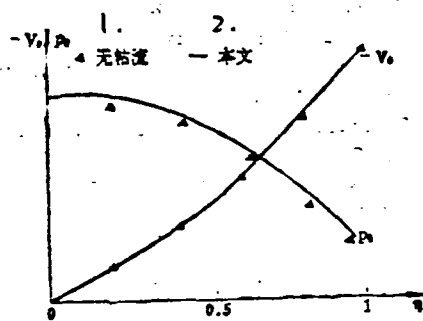Figure 4. Various ϵ_2 vs. u_1 Curves

46

Figure 5.   Gas Equilibrium Results

1.   inviscid flow
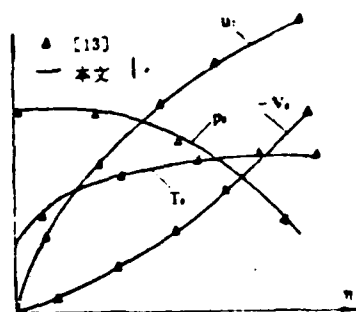2.   this work

Figure 6.   Gas Equilibrium Results

1.   this work
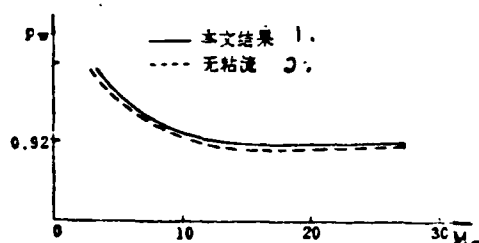
Figure 7. Body Surface Pressure vs. M_∞

      1. this work
      2. inviscid flow

Figure 7 shows a comparison of body surface pressure obtained by using this method to that calculated from an ideal gas stagnation solution over a wide range of M_∞. Obviously, the body surface pressure of a viscous flow is higher than that of an inviscid flow when the wall is cold. This means that the effect of viscosity causes the body surface to rise.

Table 2 shows the variations of the shock wave separation distance ϵ and body surface pressure p_w with Reynolds number Re_∞ at $M_\infty=20$. With increasing Reynolds number, ϵ and p_w are approaching their corresponding inviscid flow values.

Table 2 Shock Wave

Re_∞	ε	p_w
6000	0.1274	0.9214
80000	0.1297	0.92057
100000	0.1298	0.92055
1000000	0.13035	0.92051
∞	0.1304	0.92045

1. parameter

The viscous shock layer model appears to be applicable over a wide range of Re_∞. Based on our analysis, it is not reasonable to neglect the effect of downstream flow on the stagnation point when the viscous shock layer model is used to independently determine the solution in the stagnation region. In order to overcome this shortcoming, the method introduced in this paper is simple and effective.

References

[1] Wang Ruquan et al, Acta Mechanica, 3 (1980), 226-231.

[2] Golovachev, Yu.P., et al. ZhVMMF, 13, 4(1973),1021-1028.

[3] Kao, C.H., AIAA J. 2, 11 (1964).

[4] Cheng, H.K., IAS Paper, 63-92, (1963).

[5] Kaiser, J.E. et al., AD-669578, (1968).

[6] Talbot, L., Rarefied gas dynamics, (1961).

[7] Predvoditelev,A.N., et al. Tables of thermodynamic functions of air. Moscow, Izd. AN SSSR (1957).

[8] Predvoditelev,A.N., et al. Ibid, (1959)

[9] Predvoditelev, A.N., et al. Ibid (1962).

[10] Davis, R.T., AIAA J. 8, 5 (1970).

[11] Voronkin,V.G. Izv. AN SSSR, MAhG, 6(1974), 99-105.

[12] Davis, R.T. et al., AIAA J. 14, 2 (1976).

[13] Liu Xuezong et al, Numerical Computation and Computer Applications, 3 (1980).

NUMERICAL METHOD OF VISCOUS SHOCK-LAYER
NEAR THE STAGNATION LINE OF A BLUNT BODY

Yu Qingwen   Wang Ruquan
(The Computing Center, Academia Sinica)

Abstract

This paper gives a numerical solution of the viscous shock-layer equations described the flow near the stagnation line of a blunt body. The difference from usual treatments is that authors consider the influence of down-stream flow on the stagnation line and it is characterized by the boundary conditions. In this case an unknown parameter which depends on the shock wave is approximated by inviscid flow data. Numerical results agree with those given by the solution of the whole flow field in front of the blunt body.

The Perfection and Application of the Flutter Subcritical Response Analysis

Lu Qizheng, Lu Guobao and Zeng Weiqin

(China Aerodynamic Research and Development Center)

I. Introduction

In 1979, we first used a random decrement method to analyze the subcritical flutter response[1] and solved the fundamental problem to eliminate the effect of wind tunnel noise. It was pointed out in reference [1] that in order to perfect the analytical method and to put it into practical use we had to:(1) reduce running time; (2) realize on-line analysis and;(3) separate modes of closely spaced frequencies. To this end, an on-line analysis system was built between 1980 and 1981 to realize on-line analysis. Furthermore, the running time of a velocity pressure gradient was reduced from 3 minutes to 15 seconds and a curve fitting method capable of separating the subcritical response of flutter modes of two closely spaced frequencies was established. In addition, the accuracies of measurement and analysis of the subcritical response were investigated. This method was applied to various models with satisfactory results.

II. On-Line Analysis System

This system is composed of a tape recorder, a power filter, a JCD-474 detector and a DJS-21 computer. After each run, it

51

performs a random decrement analysis. By single mode curve
fitting, the frequency f and relative damping coefficient γ of
the flutter are given to instruct the continuation of the
experiment. In addition, a power spectrum analysis is performed
to determine whether the filter band selected is appropriate.
The so-called random decrement method involves the use of the
same voltage U_0 (representing the initial displacement of the
mode) to sample N sections in the modal response time process
with appropriate filtering. Then, the sum is averaged to
eliminate the effect of wind tunnel noise. The instantaneous
response of the mode remains to subsequently find γ and f.

(1) Sampling Method

In 1979, when the analysis was done on the Model CF-700
statistical analysis equipment, because we did not use a special
software package, samples were gathered after triggering by a
constant voltage U_0. Thus a larger data file was required. The
running time for each velocity pressure gradient was as long as 3
minutes. Currently, we are using an overlapping sampling method
which treats every data point "greater or equal to U_0" as the
beginning of a sample. In addition, the raw data are stored in
the memory of the computer prior to performing the computation.
Thus, the data gathered over 9 seconds can meet the accuracy
requirement. The actual running time is reduced to 15 seconds.

(2) Selection of Analytical Parameters

This is an area already covered in reference [1] and only
some additional comments are made here. If U_0 is too small, then

there are

more intersects in the response time period. The cumulative   /67

number of average is larger which favors the elimination of the

effect of noise. However, because the average amplitude of

response is lowered, the signal to noise ratio is also reduced.

Therefore, there is an appropriate range of U_0 . After many

trials, U_0 was chosen to be 1.25 times the mean square root of

response σ. In addition, comparing using "greater or equal to U_0

" as the initial condition to using "equal to U_0" as the initial

condition, we found that N could be increased by more than one

fold at the same record length. This also favors the elimination

of the effect of noise. When determining the number of samplings

n for each specimen, in addition to the fact that the random

decrement label should at least contain 6 waveform cycles, we

must also consider the frequency resolution Δf requirement for

spectral analysis ($\Delta f=(1/n\Delta t)$, where Δt is the interval between

samplings. The larger the cumulative average number N is, the

smaller the effect of noise becomes. However, the length of the

record required and the running time are also longer. Therefore,

it is necessary to choose it properly. After the sampling rate

$1/\Delta t$ and U_0 are selected, the length of the sampling time

reflects the magnitude of the cumulative average number. It was

found that, when $U_0=1.25\sigma$ and $(1/\Delta t)=1000$ cycles/sec, relatively

stable results could be obtained with a 9 second sampling time.

53

(3) Fitting of markers

Characteristically, the initial slope of every marker is zero. Thus, in order to simplify the operation, we used $Ae^{-\tau \omega t}\cos \omega t$ for curve fitting. When the signal to be analyzed only contains a single mode, such a fitting can result in relatively accurate results. If the signal contains two modes, although this fitting is not too accurate, yet it is still capable of reflecting the modal variation and the extent of approaching the critical flutter point with varying velocity pressure. It is still useful in experiments for online monitoring. As for more accurate results, a power function curve fitting method suitable for two modes can be used afterwards.

III. Curve Fitting Method

In order to process the random decay label of two mixed modes (also possible for processing single mode), a curve fitting program written in FORTRAN was compiled for a DJS-8 computer. The important features of this method are:

A complex function f is used to fit a label y from the DJS-21 computer.

$$f = \sum_{j=1}^{J} e^{-\gamma_j \omega_j t}\,(a_j \sin \omega_j t + b_j \cos \omega_j t) \tag{1}$$

$$t=t_K=K\Delta t \qquad (K=1,\ 2,\dots \dots,n)$$

where ω_j and γ_j are the characteristic frequency and damping coefficient of the jth mode to be determined, a_j and b_j are the coefficients to be determined, Δt is the interval between sampling, and K is the sequence of the data points in the label. For a dual mode system, J=2. The set of parameters to be solved is $\{a_i\}$, i=1,2,......,m. Let $a_1 = a_1$, $a_2 = -\gamma_1 \omega_1$, $a_3 = \omega_1$, $a_4 = b_1$, $a_5 = a_2$,........

The fitting is done by using the least square method to minimize the residual square sum of the fitting function f and the label y

$$R = \sum_{K=1}^{n} [y(K\Delta t) - f(K\Delta t)]^2 \tag{A}$$

i.e.,

$$\partial R/\partial a_i = 0 \quad (i=1,\ 2,\ \dots\dots,m) \tag{2}$$

Let us use a set of approximate parameters $a_i^{(0)}$ and

$$a_i = a_i^{(0)} + \Delta i \quad (i=1,2,\dots\dots,m) \tag{3}$$

Then, the problem to find $\{a_i\}$ becomes the problem to determine the correction terms $\{\Delta i\}$. By expanding f around $a_i^{(0)}$ into a Taylor series and neglecting higher terms we get

$$f(tK, a_1, a_2, \cdots\cdots, a_m) \approx f_{K_0} + \frac{\partial f_{K_0}}{\partial a_1}\Delta_1 + \frac{\partial f_{K_0}}{\partial a_2}\Delta_2 + \cdots\cdots + \frac{\partial f_{K_0}}{\partial a_m}\Delta_m \tag{4}$$

/68

where

$$f_{K_0} = f(t_K, a_1^{(0)}, a_2^{(0)}, \cdots\cdots, a_m^{(0)})$$

$$\frac{\partial f_{K_0}}{\partial a_i} = \frac{\partial f(t, a_1, a_2, \cdots\cdots, a_m)}{\partial a_i}\bigg|_{\substack{t=t_K \\ a_1 = a_1^{(0)} \\ \vdots \\ a_m = a_m^{(0)}}} \tag{A}$$

The normal equations are obtained from equation (2). Furthermore, we introduced a damping factor v into diagonal elements of the coefficient matrix in order to relax the selection requirement of the initial values $a_i^{(0)}$ and to improve the convergence of iteration. The equations are written as

$$\tag{5}$$

$$\begin{cases} (a_{11}+v)\Delta_1 + a_{12}\Delta_2 + \cdots\cdots\cdots + a_{1m}\Delta_m = a_{1v} \\ a_{21}\Delta_1 + (a_{22}+v)\Delta_2 + \cdots\cdots\cdots + a_{2m}\Delta_m = a_{2v} \\ \cdots\cdots\cdots\cdots \\ a_{m1}\Delta_1 + a_{m2}\Delta_2 + \cdots\cdots\cdots + (a_{mm}+v)\Delta_m = a_{mv} \end{cases}$$

where

$$a_{ij} = \sum_{K=1} \frac{\partial f_{K_0}}{\partial a_i} \cdot \frac{\partial f_{K_0}}{\partial a_j}, \qquad (i, j = 1, 2, \cdots\cdots, m)$$

$$a_{iv} = \sum_{K=1} \frac{\partial f_{K_0}}{\partial a_i} [y(K\Delta t) - f_{K_0}] \tag{6}$$

55

After the label is given, $a_i^{(0)}$'s are first selected. Then, the coefficient matrix and the right hand side of equation (6) are used to solve Δi by using the Gaussian elimination method in order to obtain a_i. Let $\varepsilon_i = (\Delta_i/a_i)$, $(i=1,2,......m)$. The corrected a_i is used as the initial value $a_i^{(0)}$ in the next iteration. This process is repeated until $|\varepsilon_i| < \varepsilon$ (which is a pre-determined small number). The last a_i obtained is the system parameter.

In order to further improve the converging rate, an added optimal step factor ρ_μ is also used. If the 1th iteration does not converge, it is re-defined as

$$a_i^{(1+1)} = a_i^{(1)} + \Delta_i^{(1)} \cdot \rho_\mu \qquad (B)$$

In order to improve the accuracy, the label was standardized prior to fitting.

IV. Accuracies of Analysis and Measurement

An experimental study on the accuracy of the subcritical flutter response was carried out using the flutter model of the C_2 wing. First, we investigated the statistical accuracy of the subcritical response analysis. The signal recorded for each run was analyzed 10 times for subcritical response and the mean value γ and mean square deviation σ_γ of the damping coefficient $\bar{\gamma}$ were obtained:

$$\bar{\gamma} = \frac{1}{n} \sum_{i=1}^{\bullet} \gamma_i$$

$$\sigma_\gamma = K \cdot \sqrt{\frac{1}{n-1} \sum_{i=1}^{\bullet} (\gamma_i - \bar{\gamma})^2} \qquad (C)$$

where
$$K_s = \sqrt{\frac{n-1}{2} \frac{\Gamma\left(\frac{n-1}{2}\right)}{\Gamma\left(\frac{n}{2}\right)}}$$

/69

$n = 10$

(see reference [2])

In addition, if we assume the confidence rate a=0.95, the confidence region for γ is defined as $(\bar{\gamma}-t, \bar{\gamma}+t)$:

$$t = \frac{s_1}{n} t_a$$

$$s_1 = \sqrt{\frac{1}{n-1} \sum_{i=1}^{n} (\gamma_i - \bar{\gamma})^2}$$

where t_a can be looked up in Appendix 4 in reference [2] based on the degrees of freedom K=n-1 and the confidence level a.

Results of the statistical analysis are shown in Tables 1 and 2. The γ and f for model Y1-0000 were obtained by an on-line analysis system. The γ and f for model Y2-DDDD were obtained from curve fitting of labels recorded by an on-line analysis system. In both examples, the standard deviation $\sigma\gamma$ of the damping coefficient and the amplitude of the confidence region t are relatively small, except for the second order values of the model Y1-0000. This indicates that the subcritical response analysis system, including on-line analysis and curve fitting, has a satisfactory accuracy to meet the needs of model testing.

57

Table 1. Statistical Analysis of Accuracy of the C_2 Wing Model (Y1-0000, 637 runs)

M	q (kg/m²)	$\bar{f}$ (Hz)	$\bar{\gamma}$	σ_γ	t
0.911	5204	66.19	0.0658	0.00334	0.00244
0.911	5699	70.97	0.0495	0.00678	0.00495
0.911	6197	72.78	0.0237	0.00183	0.00133
0.911	6572	73.69	0.0164	0.00120	0.00120
0.912	6789	74.45	0.0061	0.00036	0.00027

Table 2. C_2 Wing Model with Missiles (Y2-DDDD, 526 runs)

M	q (kg/m²)	$\bar{f}$ (Hz)	$\bar{\gamma}$	σ_γ	t
0.877	3734	42.75	0.01667	0.000326	0.000238
0.881	3913	42.69	0.00951	0.000348	0.000254
0.885	4069	42.67	0.00672	0.000324	0.000244
0.894	4309	42.18	0.00475	0.000261	0.000191
0.898	4493	41.86	0.00353	0.000317	0.000161
0.902	4683	41.78	0.00283	0.000354	0.000354

For the same model state (Y1-0000), six runs were performed in repetition. The average of 10 analyses is used as the "measured value" for each run. The least square method is used to determine the critical flutter velocity pressure q_{kp}, by extrapolation. The relative value of the standard deviation of the critical velocity pressure between runs $^\sigma q_{kp}$ to the mean critical velocity pressure $\bar{q}_{kp}$ is determined as follows:

$$^\sigma q_{kp}/\bar{q}_{kp} = 1.30\% \qquad (C)$$

The relative value of the maximum deviation of the critical velocity pressure is

$$q_{kpmax}-\bar{q}_{kp}/q_{kp} = 2.30\% \qquad (A)$$

which indicates that the reproducibility of the measurement can satisfy the requirement of the model experiment.

V. Application Results

(1) Transonic Flutter Model of Model A Wing. The experiment was carried out in a 0.6 meter transonic wind tunnel. Figure 1 shows the $\gamma{\sim}q$ curve obtained by various analysis systems at M=0.75. An after the fact analysis method was used in this experiment. The critical velocity pressure obtained by extrapolation using the subcritical method differs from the directly measured value by less than 8%.
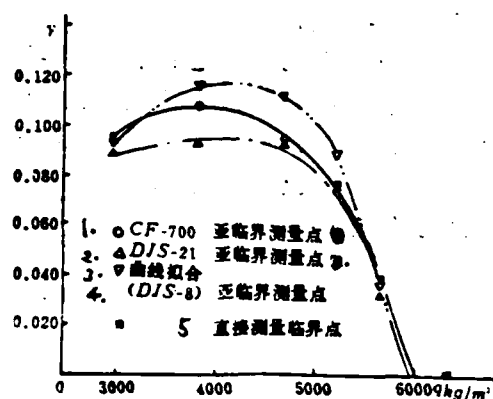
Figure 1. Relative Damping Coefficient vs. Velocity Pressure
for a Model A Transonic Wing (M=0.75)

1. oCF-700 subcritical measured points
2. ΔDJS-21 subcritical measured points
3. ∇curve fitting
4. (DJS-8) subcritical measured points
5. directly measured critical points

(2) Low Velocity Flutter for Model B Aircraft. The

experiment was carried out in a 4mx3m low velocity wind tunnel.

In the case of a 15 ton commercial load, 0303 hoist, no fuel, and

with symmetric flutter, because the critical flutter point does

not appear up to the allowed wind speed of 58m/sec, we can only

rely on extrapolation based on the subcritical method. For both

modal states, all labels showed a beat resonance effect due to

the mixing of two closely spaced frequency modes. Therefore, it

is necessary to go through curve fitting. The resultant γ-q

curve for the flutter mode is shown in Figure 2. We can see that

60

the critical flutter velocity determined with the subcritical

method is in good agreement with the directly measured value and

the theoretical value.

(3) Supersonic Flutter Model of 60° Delta Flat Wing. The

experiment was performed in a 0.6 meter supersonic wind tunnel.

The M numbers were 1.5, 2.0 and 2.5. It was discovered in the

experiment that the model exhibited a near sinusoidal, but

slightly damped vibration over a wide velocity pressure range.

It was difficult to directly measure the critical point. For

this reason, the subcritical response $\gamma{\sim}q$ curve shown in Figure 3

was used to determine the critical point by defining the turning

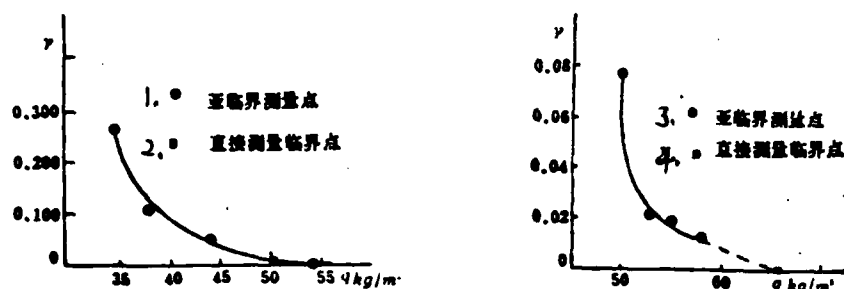point at which γ becomes small ($\gamma<0.01$) and flat.

Figure 2. Relative Damping Coefficient vs. Velocity for Low
Velocity Model B Wing

1. subcritical measured point
2. directly measured critical point
3. subcritical measured point
4. directly measured critical point

61

(4) Transonic Flutter Model C Wing. The experiment was carried out in a 0.6 meter transonic wind tunnel. Typical results are shown in Figure 4. In this experiment, an on-line analysis on the subcritical response was performed. The critical points obtained by extrapolation using the subcritical method are within 2% of directly measured values. As compared to the 8% deviation in the off-line analysis of Model A, because on-line analysis enables the measured point to get closer to the critical point, extrapolated results are more accurate.
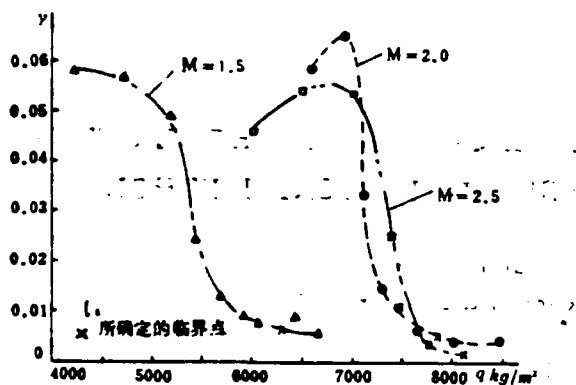

Figure 3. Relative Damping Coefficient vs. Velocity Pressure for a Delta Flat Supersonic Wing
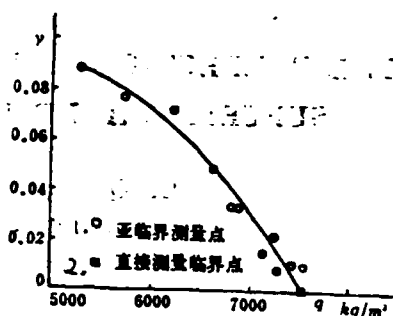1. determined critical point

Figure 4.   Relative Damping Coefficient vs. Velocity Pressure
            for Model C_1 Transonic Wing $M = 0.866$

            1.   subcritical measured point
            2.   directly measured critical point

(5)   Transonic Flutter of C_2 Wing with Missiles.   The
experiment was carried out in a 0.6 meter transonic wind tunnel.
Because the subcritical method was used, more experimental
results were obtained with each model, including the comparison
of the critical flutter velocity pressure at various hanging
positions and the effect of transonic compressibility of Y2-DDDD.
This fully demonstrates the superiority of this method.   The
subcritical analysis of the typical Y2-DDDD model is shown in
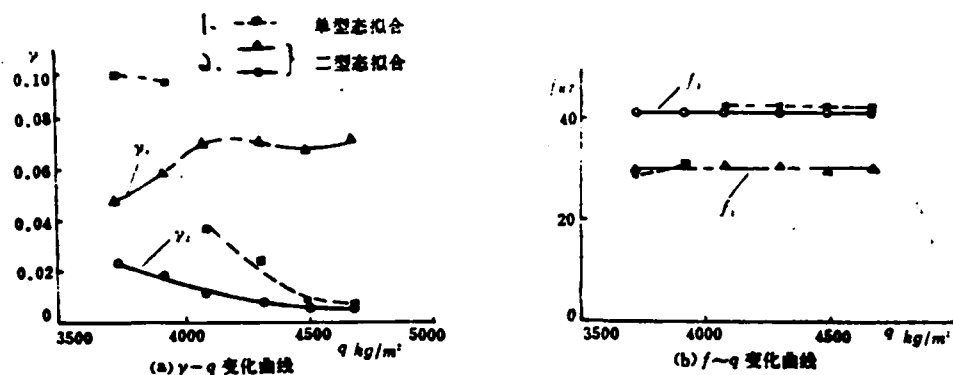Figure 5.

63

Figure 5.   Relative Damping Coefficient vs. Velocity Pressure
for Model C_2 Wing with Missiles (M=0.866)

1.   single mode fitting
2.   dual mode fitting
(a) γ-q curve
(b) f-q curve

VI.   Conclusions

The subcritical flutter response analysis based primarily on
a random decrement with power spectral analysis is a successful
one.   The power spectrum method is effective in determining the
mode of analysis and filter bandwidth.   In the event that two
closely spaced frequencies are mixed, curve fitting is
imperative.   The establishment of an on-line analysis system can
improve the accuracy of measurement and reduce the running time.
This method can be used in transonic, supersonic and low speed
flutter experiments.

References

[1] Lu Qizheng, Journal of Aerodynamics, 1 (1980).

[2] Shen Hengfan, Lecture Note on Probability, People Education
Publishing Co., 1966.

THE PERFECTION AND APPLICATION OF THE FLUTTER
SUBCRITICAL RESPONSE ANALYTICAL METHOD

Lu Qizheng   Lu Guobao   Zeng Weiqin
(China Aerodynamic Research & Development Center)

Abstract

The Random Decrement/Power Spectrum subcritical response analytical method was used recently in the wind tunnel model flutter test. This paper describes the perfection and application of the method, and includes the establishment of the on-line analytical system, the establishment of curve fitting method with exponential functions, the study of accuracy, and the results from application of the method. The method has follwing features, the effect of the wind tunnel flow noise can be eliminated effectively, the running time is shorter, the modes of closely space frequencies can be identified. Its feasibility is good. The practical application in the tests of Model A, B, C and a 60° delta flat wing model shows that the method can be applied to transonic, supersonic and low speed wind tunnel flutter tests.

Calculation of Octagonal Wall Interference Factor Using

Conformal Mapping

(Northwestern Polytechnical University)

I. Introduction

Currently, the cross-section of many low velocity wind tunnels is octagonal. Furthermore, the δ curve given in references [3] and [6] is used for wall correction.

There are primarily two methods to determine the value of δ: one is the image method which is capable of calculating the δ values for circles, squares, rectangles, ellipses and the other is conformal mapping which is capable of calculating the values of δ for rectangles, squares, ellipses and octagons. However, based on information available to date, we still could not find an accurate formula to calculate the interference factor for an octagonal wall based on the two methods mentioned above. The methods used in papers discussing this problem are appropriate. The method in this work, however, can provide an accurate formula for calculation. In addition, this method is also much simpler than those approximation methods. It is capable of calculating the δ values for rectangles, squares and octagonal wall interference factors.

In the following calculation, let us assume that the wing load is uniform, i.e., the wing is replaced by a pair of vortices. In addition, it also assumes that the wing is located in the plane of symmetry in the test section of the wind tunnel.

66

II. General Equation for Calculating Wall Interference

Factor of Any Shape Using Conformal Mapping. The interference of a circular-section wall can be easily resolved. It is natural to think that whether this problem can be resolved if the conformal mapping formula for transforming the inside of an arbitrary wind tunnel to a circular-section is known. This problem had been proven in reference [1].

Let us assume that the following transformation formula

$$\xi = f(Z) \tag{2.1}$$

can transform the cross-section of a specific wind tunnel into a unit circle $|Z|=1$ on the Z plane by conformal mapping. Furthermore, the mapping is conformal for every point. Let us assume that the wing in the tunnel is replaced by a pair of vortices $(\Gamma,-\Gamma)$ spaced by b (the wing span), as shown in Figure 1.

If the vortices are located at ξ_1 and ξ_2 on the ξ plane, they are transformed to Z_1 and Z_2 on the Z plane without changing its intensity[1].

Based on reference [1], when the wing is located on the real axis and the center of the wing span is at the origin, if the interference angle at the center of the wing span is used to represent the value on the entire wing, then the value of δ is:

$$\delta = \frac{A_v}{2\pi b^3} \left\{ 1 - \frac{b}{2f'(0)} \left(\frac{2}{l} - \frac{l}{2} \right) \right\} \tag{2.2}$$

where A_W is the cross-sectional area of the experimental section of the wind tunnel.

When the span is large relative to the dimension of the experimental section of the wind tunnel, it is more appropriate to use the average interference angle along the wing span. In this case, we get:

$$\delta = \frac{A_w}{16\pi \left(\frac{b}{2}\right)^2} \log \frac{\frac{b}{2}\left(\frac{l}{2}+\frac{2}{l}\right)}{f'\left(\frac{l}{2}\right)\left(\frac{2}{l}-\frac{l}{2}\right)\frac{l}{2}} \qquad (2.3)$$

III. Conformal Mapping Formula from Unit Circle to Octagon

It was given in reference [2] that

$$\zeta = \int_0^z (Z-a_1)^{\alpha_1-1}(Z-a_2)^{\alpha_2-1}\cdots\cdots(Z-a_n)^{\alpha_n-1}dZ \qquad (3.1)$$

where α_K (K=1,2,......,n) - apex angles of the polygon in the unit of π.

α_K (K=1,2,......,n) - points on the unit circle corresponding to apices.

From Figure 2 one can see that A', B', C', D', E', F', G' and H' on the octagon correspond to points A, B, C, D, E, F, G and H on the unit circle.

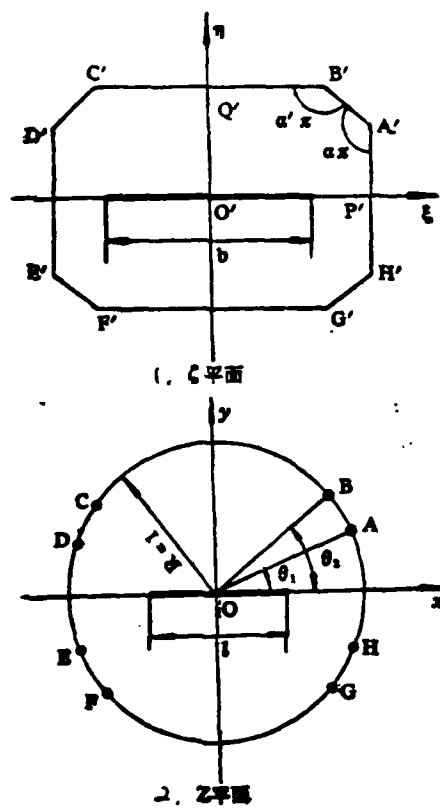| point	A	B	C	D	E	F	G	H
α_K	$e^{i\theta_1}$	$e^{i\theta_2}$	$e^{i(\pi-\theta_2)}$	$e^{i(\pi-\theta_1)}$	$e^{i(\theta_1-\pi)}$	$e^{i(\theta_2-\pi)}$	$e^{-i\theta_2}$	$e^{-i\theta_1}$

68

Figure 1. ξ Plane and Z Plane
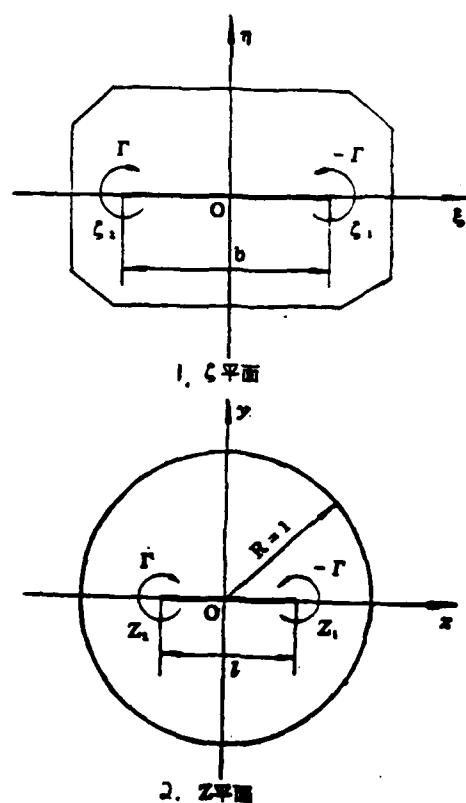
1. ξ plane
2. Z plane

1. ζ平面

2. Z平面

Figure 2.   Relation Between ξ Plane and Z Plane

1.   ξ plane
2.   Z plane

From Figure 2 one can see that the value of α_K is as follows:

$$\angle A' = a\pi, \qquad \angle B' = a'\pi, \qquad a + a' = \frac{3}{2}.$$

By substituting the α_K and α_K obtained into equation (3.1), we get

$$\zeta = \int_0^z [(Z - e^{i\theta})(Z - e^{-i\theta_1})(Z - e^{i(\pi - \theta_1)})(Z - e^{-i(\pi - \theta_1)})]^{a-1}$$
$$\cdot [(Z - e^{i\theta_1})(Z - e^{-i\theta_1})(Z - e^{i(\pi - \theta_1)})(Z - e^{-i(\pi - \theta_1)})]^{\frac{1}{2} - a} dZ \qquad (3.2)$$

70

Equation (3.2) includes three parameters: θ_1, θ_2 and α. For a specific wind tunnel, these three parameters are uniquely defined.

When α is fixed, two length ratios $(O'Q'/O'P')=A$ and $(A'P'/O'P')=B$, can be used to define an arbitrary octagonal section.

1. Calculation Formula for O'P'

From Figure 2 one can see that in this case, Z=x. Because it is a unit circle, equation (3.2) becomes:

$$O'P' = \int_0^1 [(1+x^2)^2 - 4x^2 \cos^2 \theta_1]^{\alpha-1}[(1+x^2)^2 - 4x^2\cos^2 \theta_2]^{\frac{1}{2}-\alpha}dx \qquad (B)$$

Let $\alpha = 3/4 + 1/4\beta$, $\beta=[1,-1]$. Then

$$\alpha-1=-1-\beta/4, \qquad 1/2-\alpha=-1+\beta/4 \qquad (C)$$

Substituting it into the above equation, we get

$$O'P' = \int_0^1 [(1+x^2)^2 - 4x^2 \cos \theta_1]^{-\frac{1-\beta}{4}}[(1+x^2)^2 - 4x^2 \cos^2 \theta_2]^{-\frac{1+\beta}{4}}dx \qquad (3.3)$$

2. Calculation Formula for O'Q'

From Figure 2 one can see that Z=iy. For convenience, let y=x. After substituting it into equation (3.2), we get

$$O'Q' = \int_0^1 [(1-x^2)^2 + 4x^2 \cos^2 \theta_1]^{-\frac{1-\beta}{4}}[(1-x^2)^2 + 4x^2\cos^2\theta_2]^{-\frac{1+\beta}{4}}dx \qquad (3.4)$$

3. Calculation Formula for A'P'

From Figure 2 one can see that $Z=e^{i\theta}$. After substituting it into equation (3.2) we get

$$A'P' = \frac{1}{2}\int_0^{\theta_1} [\sin (\theta_1 - \theta)\sin(\theta+\theta_1)]^{-\frac{1-\beta}{4}}[\sin(\theta_2 - \theta)\sin(\theta_2+\theta)]^{-\frac{1+\beta}{4}}d\theta \qquad (D)$$

71

On the above integral is a generalized one when $\theta \to \theta_1$. It should be treated properly. For this purpose, we introduced a new variable, i.e.,

$$(\theta_1 - \theta)^{\frac{1}{4}(3+\beta)} \equiv \xi, \text{ then } d\xi = \frac{3+\beta}{4}(\theta_1 - \theta)^{-\frac{1-\beta}{4}} d\theta \qquad (E)$$

Therefore,

$$[\sin(\theta_1 - \theta)]^{-\frac{1-\beta}{4}} = \frac{4}{3+\beta}\left[\frac{\sin(\theta_1 - \theta)}{(\theta_1 - \theta)}\right]^{-\frac{1-\beta}{4}} d\xi \qquad (F)$$

After substituting it into the expression for A'P', we get: /81

$$A'P' = \frac{2}{3+\beta}\int_0^{\theta_1^{\frac{3+\beta}{4}}}\left[\frac{\sin(\theta_1 - \theta)}{\theta_1 - \theta}\sin(\theta_1 + \theta)\right]^{-\frac{1-\beta}{4}}$$
$$\cdot [\sin(\theta_2 - \theta)\sin(\theta_2 + \theta)]^{-\frac{1-\beta}{4}} d\xi \qquad (3.5)$$

IV. Special Cases

1. Formula for Normal Octagonal Section

The formula for a normal octagonal section can be obtained by letting $\theta_1 = 22.5°$ and $\theta_2 = 67.5°$ in the above equation.

2. Formula for Rectangular Section

The formula for rectangular section can be obtained by letting $\theta_1 = \theta_2$ in the above equation. In addition, only the integrals of O'P' and O'Q' are required to be calculated when calculating the interference factor of a rectangular section because A'P'=O'Q'.

(1) Formula for O'P'

In this case, $\beta = -1, \theta_1 = \theta_2 = \theta$. By substituting these factors into equation (3.3) we get
$$O'P' = \int_0^1\frac{dx}{\sqrt{(1+x^2)^2 - 4x^2\cos^2\theta}} \qquad 4.1$$

(2) formula for O'Q'

In this case $O_1 = O_2 = 0$ and $\beta = -1$. Substituting these into equation (3.4) we get

$$O'Q' = \int_0^1\frac{dx}{\sqrt{(1-x^2)^2 + 4x^2\cos^2\theta}} \qquad (4.2)$$

72

3. Formula for square section

When O'P'=O'Q', i.e., a square, it is determined by the following formula:

$$O'P' = O'Q' = \int_{\bullet}^{1} \frac{dx}{\sqrt{1+x^4}} \qquad (4.3)$$

V. Conclusions

1. When K<0.6, the δ value of an octagonal section calculated by using this method is very close to that of an elliptical section of the same height to width ratio. When K> 0.6, the difference is larger, as shown in Figure 3.

2. The δ value of a regular octagon calculated by using this method is identical to those reported in the literature, as shown in Figure 4.
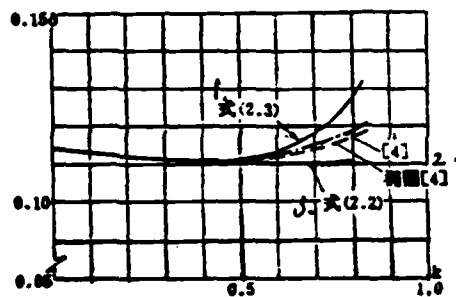
Figure 3.   Comparison of δ Values of Octagonal Sections
(λ=wind tunnel height/width =0.778 and k=wing span/ wind tunnel width)

    1.   equation (2.3)
    2.   ellipse in reference [4]
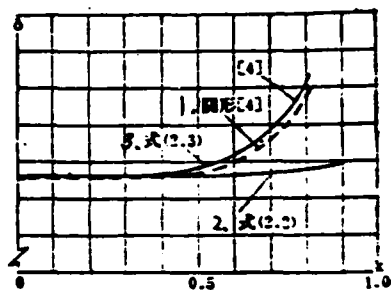   3.   equation (2.2)

73

Figure 4.   Comparison of δ Values of Octagonal Sections

    1. circle in reference [4]
    2. equation (2.2)
    3. equation (2.3)

3.   It is suggested that this method be used to calculate   /82
the corresponding curve for a given octagon, instead of the curve
derived in references [3] and [6].

                              References

[1] Milne-Thomson, L.M., Theoretical Aerodynamics, 1952.

[2] Lafuzanjiefu, M.A., Complex Function Methods, 1957.

[3] Alon Pope, John J. Harper, Low Speed Wind Tunnel Testing,
     1966.

[4] Fan Jiechuan, Correction for Octagonal Wind Tunnel Wall
     Interference, 7210 Journal, 1, (1978).

[5] Xia Yushun, Using Conformal Mapping to Calculate the
     Wall Interference Factor for an Octagonal Wind Tunnel,

74

Science and Technology Information, Volume 199, North-
western Polytechnical University, 1974.

[6] Pengkesiter, R.C., and Hert, D.W., Wind Tunnel Experi-
mental Techniques, Defense Industry Publishing Co., 1963.

WALL-INTERFERENCE CALCULATION OF WIND TUNNEL WITH OCTAGONAL SECTIONS USING CONFORMAL MAPPING METHOD

Xia Yushun and Lin Chaoqiang
(Northwestern Polytechnical University)

Abstract

. The conformal mapping formula is used for the wall-interference calcul-
ation of wind tunnel with octagonal sections. The parameters in the
mapping formula can be easily determined by computer. As particular
examples, the results for rectangular, square and regularoetagon sections
are also given in closed form. Some typical results are plotted and com-
pared with other results.

Cryogenic High Reynolds Number Transonic Wind Tunnel with Pre-cooled and Restricted Flow

Pan Ruikang

(China Aerodynamic Research and Development Center)

Introduction

Since the sixties, many foreign countries were concerned about the problem of insufficiently low Reynolds numbers in wind tunnel experiments which seriously affected the performance of aircraft. Due to insufficiently low Reynolds numbers, areas in aerodynamics primarily caused by viscosity and certain aerodynamic phenomena with strong coupling of viscous surface flow and inviscid external flow cannot be simulated. Therefore, aerodynamic researchers proposed that the entire range of Reynolds number encountered in flight should be simulated in the wind tunnel. NATO countries and the U.S. organized special task teams to study this problem. Several high Reynolds number transonic wind tunnels have been developed, including the low temperature nitrogen wind tunnel, Ludvic tube wind tunnel, jet wind tunnel and Evans wind tunnel.

Historically, Osborne Reynals began by focusing his attention on the effect of low temperature gas on flow characteristics. In addition, low temperature experiments were done and a suggestion to lower air temperature was made. In 1920, William Margoulis (NACA) was the first one to introduce the concept of low temperature wind tunnels to consider the effect of pressure, temperature and the experimental gas on the aerodynamic

experiments. In 1945, in order to reduce the power of high speed wind tunnels and to improve the economics, Smelt suggested that the gas and temperature should be appropriately chosen. Due to various reasons, low temperature gas did not receive any attention[1]. In 1977, Storllery in England introduced the idea of using the adiabatic expansion of air stored in a high pressure container to obtain the low temperature desired. In the experiment, the control of a piston movement is used to maintain the temperature and pressure at the stagnation point[2]. In 1979, Curt Nelander of Sweden introduced a new scheme in the first international discussion meeting of low temperature wind tunnels. In his scheme, a compressor is used to compress the gas exhausted from the wind tunnel which is stored in the low temperature pipe underground. A portion of the compressed air is stored in a high pressure vessel and another portion, approximately 38%, passes through an air cooling device. In the experiment, the air in the high pressure vessel, after adiabatic expansion and throttling is mixed with low temperature air to ensure that the required temperature and pressure are attained in the stable section of the wind tunnel. In 1980, Lian Qixing of Beijing Institute of Aeronautics and Astronautics introduced a plan to use heat exchangers for cooling[4]. In this scheme, the air in the high pressure storage system is adiabatically expanded to allow the heat reservoir to attain the desired low temperature. In this experiment, medium pressurized air passed through the heat reservoir to reach the desired low temperature.

Since 1975, we surveyed various high Reynolds number, Re, wind tunnels. Primarily we believe that the cryogenic nitrogen wind tunnel, particularly continuous low temperature nitrogen wind tunnel such as NTF of NASA, is more desirable among various high Re number wind tunnels. Because of the high investment of building such a wind tunnel, it is significant to seek new technical approaches. This paper describes one such approach.

Although the cryogenic high Re number wind tunnel with pre-cooled and restricted flow introduced in this paper still have some technical difficulties in high pressure low temperature engineering, however, it is relatively easier as compared to other cryogenic air wind tunnels. Because of the pre-cooling and flow restriction, not only the experience gathered in the construction and operation of the gas storage systems of hypersonic wind tunnels and the experience acquired in the use of intermittent wind tunnels can be applied, but also the cost of building such wind tunnels is much lower than that of a nitrogen cryogenic wind tunnel. Based on the pre-cooling and flow

restriction approach, this paper introduces a 2.4m high Re number/88 cryogenic transonic wind tunnel.

Cooling System for Pre-cooling and Flow Restriction

The temperature of air can be lowered by heat transfer through a medium or by refrigeration[5]. Because a pressure regulating valve is used to exhaust a large amount of stored air

78

in an intermittent wind tunnel, therefore, the experimental process itself is a refrigerator process for air. The adiabatic expansion of stored gas and restriction of flow by the pressure regulating valve is used to refrigerate the air to a low temperature. Although the temperature lowering effect due to flow restriction of the valve can be calculated, however, it is more convenient to look it up in the temperature-entropy plot from an engineering point of view[6],[7]. Because the pressure of stored gas in a transonic wind tunnel is relatively low, the temperature drop due to the integrated flow restriction effect is small. However, the temperature drop caused by the adiabatic expansion in the gas storage vessel is large. In order to avoid this temperature drop effect, a heat reservoir is stored in the container to control the temperature drop.

The adiabatic expansion or air in a container or flow restriction by a throttle, or both can be used to refrigerate the cryogenic wind tunnel itself. Plans introduced by Stollery and Nelander require the use of complicated systems to control fluctuations of temperature and pressure at the stagnation point. In this aspect, pre-cooling with flow restriction and adiabatic expansion are relatively simple. The following is a comparison of these two plans.

Figure 1 shows an adiabatic expansion cooling system. Air from the atmosphere or in 10 atm containers is compressed to 175 atm and stored in vessels. The valve A is opened to allow the air from the high pressure vessel to expand adiabatically to

lower the pressure from 175 atm to 10 atm. Then, valve A is
closed. In the experiment, the flow restricting valve controlled
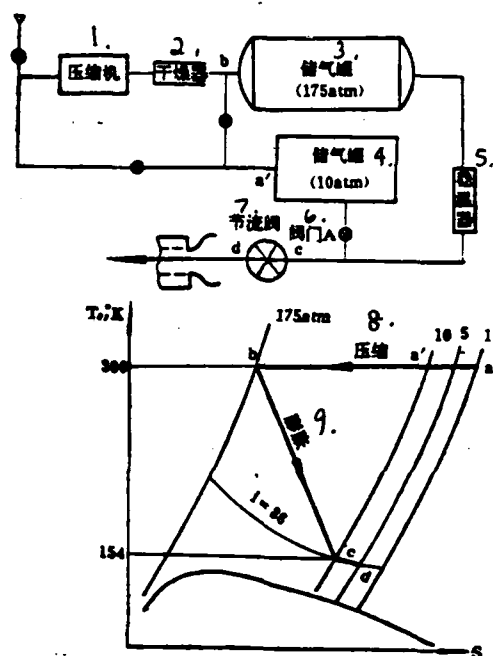the air to reach state d (5 atm, 154 atm).

Figure 1. The Adiabatic Expansion Air Cooling System and the
Temperature vs. Entropy Curve

1. compressor
2. drier
3. gas storage vessel (175 atm)
4. gas storage vessel
5. temperature stabilizer
6. valve A
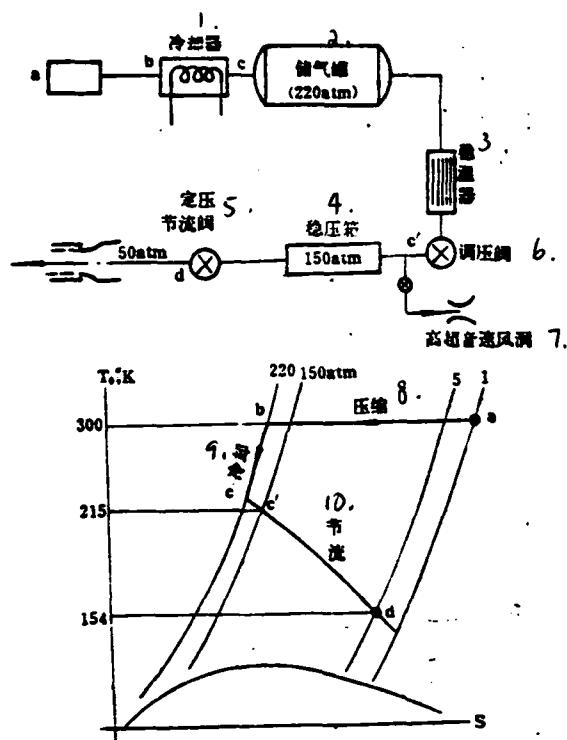7. throttle valve
8. compression
9. expansion

Figure 2.　The Pre-cooled and Flow Restricted Air Refrigeration
　　　　　　System and the Temperature vs. Entropy Curve

1.　cooling unit
2.　gas storage vessel
3.　temperature stabilizer
4.　pressure stabilizer
5.　isobaric throttle
6.　pressure regulating valve
7.　hypersonic wind tunnel
8.　compression
9.　cooling
10.　flow restriction

Figure 2 shows the pre-cooled, flow-restricted refrigeration

system, the gas undergoes the processes of compression (a-b),

cooling (b-c), isothermal pressure reduction (c-c') and flow

restriction (e'-d).　The compressor compresses the air to 220　　/89

81

atm. It is then cooled to 215K by passing through the refrigerator. It is finally stored in a high pressure vessel. In the experiment, the pressure regulating valve and the isobaric flow throttle are opened simultaneously. The former keeps the pressure stabilizing box at 150 atm at all times and finally maintains the stagnation pressure in the stabilized section in state d. The pre-cooling system in the system is a conventional cooling unit, which may be a freon refrigeration system or a flow-restricted pre-cooling system or an exhaust gas pre-cooling system.

The choice of either refrigeration plan should be made based on technical difficulties and experimental requirements. It should also take factors such as energy consumption, capital cost, and experimental expenses into account. Table 1 shows a comparison of these two systems in a transonic wind tunnel with a 2.4m x 2.4m experimental cross-section. From the table one can see that the storage vessel in the air expansion system is 3×10^5 m^3 which is impossible to materialize in practice. Although Stollery's plan was improved, however, it still requires a considerably large volume. Thus, it is difficult to control the piston. Nelander's plan was indeed a significant improvement. However, it is difficult to control the temperature and pressure of the flow in the stable section. On the contrary, pre-cooled flow-restricted refrigeration systems, no matter whether pre-cooled or temperature and pressure controlled, can be realized from an engineering point of view. The gas supply system is

similar to that of a hypersonic wind tunnel. In this case, this
system can be shared with a hypersonic wind tunnel. Not only the
technical difficulty is low, but also the capital investment it
less. It is a more rational plan.

Table 1. Comparison of Adiabatic Expansion and Pre-cooled
Slow-restricted Systems

1. 项　　目	2. 绝热膨胀制冷系统	3. 预冷节流式制冷系统
4. 贮气条件	5. 气压压力 atm	175	220
	6. 中间压力 atm	10	150
	7. 终止压力 atm	5	150
	8. 起始温度 K	300	215
	9. 最低温度 K	154	215
	10. 贮气重量 T	3870	350
	11. 贮气容积米³	18000	1290
	12. 贮气余气量 T	111	240
	13. 试验时温降 K	23.6	18.1
	14. 应补偿温度 K	14	8.1
	15. 铝蓄热元件重量 T	3120	636
16. 系统可能消耗能量 kg·M		32.9×10^{10}	3.23×10^{10}
17. 主要异同设备和系统	18. 预冷系统	/	应使 300K 空气冷却到 215K
	19. 干燥器	保证空气含湿量0.0002g水/kg空气	/
	20. 降温排气贮气罐米³	30万	试验时保持 150atm 稳定
	21. 稳压箱	无	有
	22. 快速高压阀	有	无
	23. 恒压节流阀	无	有

83

1. item
2. adiabatic expansion refrigeration system
3. pre-cooled flow-restricted refrigeration system
4. gas storage condition
5. gas pressure atm
6. medium pressure atm
7. final pressure atm
8. initial temperature K
9. lowest temperature K
10. weight of stored gas T
11. volume of stored gas m^3
12. residual stored gas T
13. temperature drop in experiment K
14. temperature compensation K
15. weight of aluminum heat reservoir
16. energy consumed by system Kg.M
17. major similar and different equipment and systems
18. pre-cooling system
19. drier
20. volume of storage vessel for gas exhausted in lowering temperature m^3
21. pressure stabilizing box
22. high speed high pressure valve
23. isobaric throttle
24. to ensure the humidity in air is $0.002gH_2O/Kg$ air
25. 300,000
26. none
27. yes
28. none
29. cooling air from 300K to 215K
30. maintaining 150 atm during experiment
31. yes
32. none
33. yes

The 2.4 Meter High Re Number Transonic Cryogenic Wind Tunnel

The dimensions of the experimental section of the intermittent high Re number Cryogenic Air Wind Tunnel are 2.4m x 2.4m. The M number in the experiment is 0.5~1.6. It is required that within the range of M encountered in the experiment that the Re number is 4×10^7 with respect to a 0.24m characteristic length. That means Re=16.7×10^7 with respect to a characteristic length is one meter.

In order to realize this experimental state, stagnation pressure and temperatures at various M numbers are chosen from Figure 3. If the design state is M=0.8, then the corresponding stagnation pressure P_0 =5 atm and stagnation temperature T_0 =154K.

A wind tunnel is composed of a gas supply system, the main /90 wind tunnel and a waste gas recovery system. Figure 4 shows the variation of states in the process a-b-c-c'-d in the wind tunnel experiment. In reality, c-c' does not exist. Instead, it varies according to c-c''. In this case, the final temperature may reach 138K. From an engineering point of view, if we assume that the temperature loss along the path is equal to the cc'' flow-restricted temperature, then c-c' is selected. The process c'-d is realized by the isobaric flow restricting throttle. The final point d corresponds to the gas parameters. P_0 =5 atm and T_0 =154K in the experimental section. The total picture of the wind tunnel is shown in Figure 5.
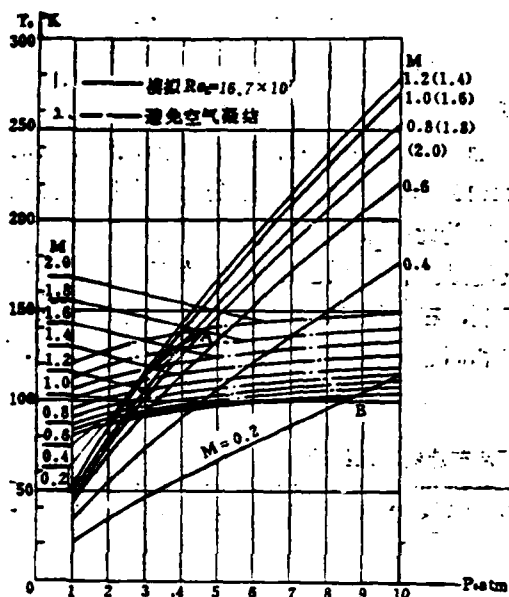
Figure 3. Stagnation Point and Temperature of Cryogenic Air
Wind Tunnel

1. simulating Re =16.7 x 10^7
2. avoid air condensation

In the gas supply system, there are five Model H22 axi-flow
air compressors. The inlet air flow is 130m^3/mm per unit and the
exhaust pressure is 220 atm. The axial power N=630KW. The air
filling time for the first experiment is 5 hours. Under designed
conditions, the filling time is 2 hours. The pre-cooling system
not only provides cooled air but also makes the humidity in the
air to be under 0.2g water/kg air. Two sets of heat exchangers
are used alternately. When one unit is operating, the other unit
is being defrosted. The volume of the high pressure gas storage

vessel is 1290m^3. It is made of 09Mn2VR low temperature steel.

The temperature stabilizing device is used to compensate the temperature drop caused by the adiabatic expansion of gas in the high pressure vessel. The initial temperature drop is estimated to be 18.1K. It is necessary to compensate 8.1K. Thus, it is required to place 530T of LF5 aluminum alloy in the temperature stabilizer. After considering the actual conduction effect, it should be increased by 20%, i.e., 636T. When designing the heat exchanger element, the contact area should be increased and the wall thickness should be decreased.

The pressure regulating valve and the isobaric throttle are important components of the system. The former can maintain the pressure in the pressure stabilizing box and the error is controlled within the range of 0.5-1.0%. The latter should maintain the pressure drop at a given M number in the experiment. Under the condition that the flow cross-section of the valve remains unchanged, the pressure fluctuation in the stable section should be less than ±0.5%. The range of adjustment of the pressure ratio of the pressure regulating valve is 0.68~1. The inlet diameter is 2m and the outlet diameter is 2.4m. The pressure ratio adjustment range of the isobaric flow restricting valve is 0.06~0.01. The inlet diameter is 2.4m. The pressure regulating ranges of these two valves are narrow. It is easy to realize flow restriction. It is feasible to use the common hole or slot acoustic damper valves.

The end of the exhaust diffusion section of the wind tunnel is equipped with a wave stabilizer which is used to control the

position of the wave to allow a stable M number in the experimental section. In the experiment, the pressure in the gas collecting vessel is increasing. The shock wave in the wave stabilizer continuously moves forward. However, the wave stabilizer can stabilize the wave downstream from the throat to maintain the aerodynamic condition for the experiment.

The exhaust gas collecting vessel collects the low temperature exhaust gas. A part of it is the coolant of the pre-cooling system and the other part is sucked into the compressor to be re-cycled. For this reason, the pressure of the gas collecting tube should not be too low. Otherwise, it must be pressurized by a pump in order to supply gas to the pre-cooling system. If the maximum pressure of the collecting vessel is 2 atm and the minimum pressure is 0.3 atm, then the total volume of the vessel must be $2.7 \sim 3.6$ m^3. If low temperature air is directly exhausted into the atmosphere, then the temperature should be raised to protect the environment.
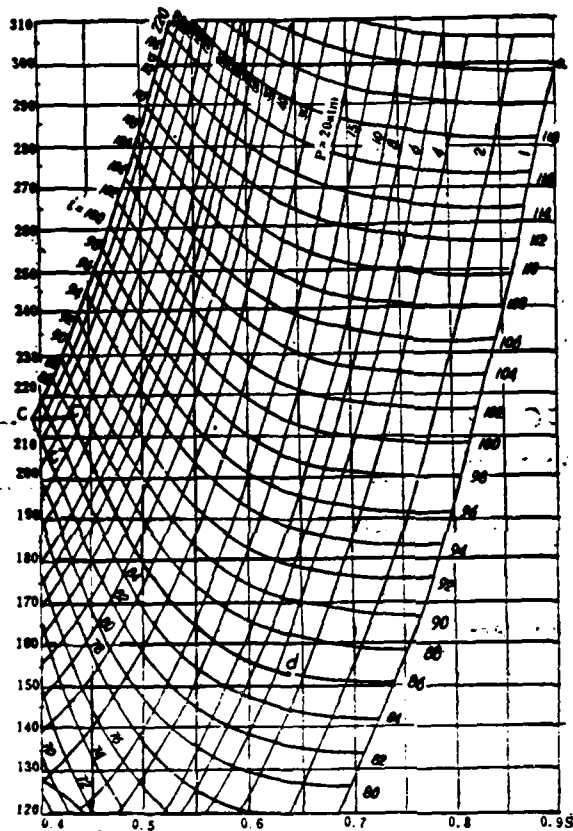
Figure 4. Variation of Gas States in a 2.4m Wind Tunnel
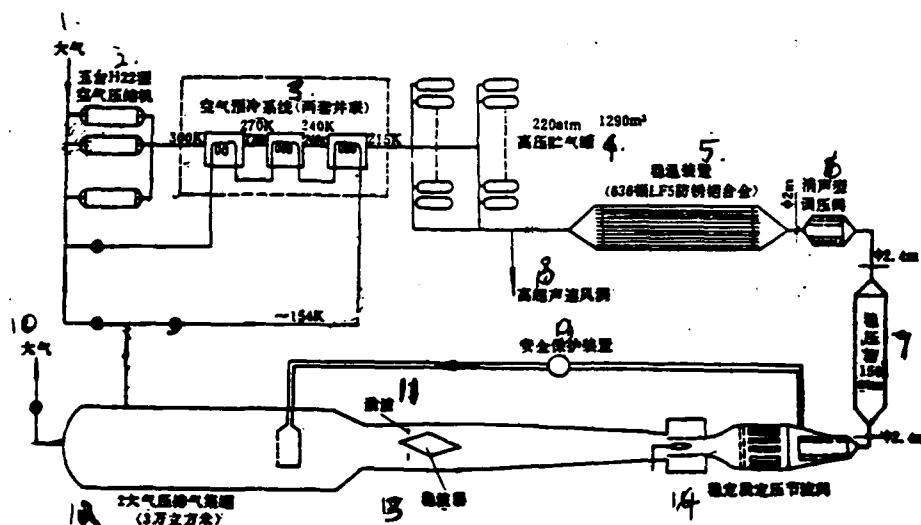
Figure 5.   A 2.4m x 2.4m High Re Number Cryogenic Transonic
            Wind Tunnel

  1.   atmosphere
  2.   five Model 22 air compressors
  3.   air pre-cooling systems (two in parallel)
  4.   high pressure gas storage vessel
  5.   temperature stabilizing device (636 tons of LF5
       corrosion resistant aluminum alloy)
  6.   acoustic damper valve
  7.   pressure stabilizing box 150 atm
  8.   hypersonic wind tunnel
  9.   safety and protection device
 10.   atmosphere
 11.   shock wave
 12.   atm exhaust gas collecting vessel (30,000m^3)
 13.   wave stabilizer
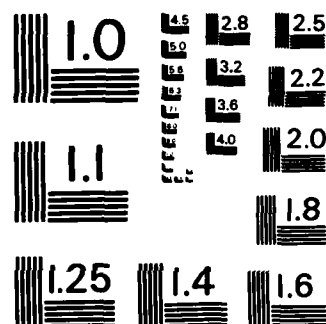 14.   isobaric flow throttle in the stabilized section

END

FILMED

DTIC

MICROCOPY RESOLUTION TEST CHART

NATIONAL BUREAU OF STANDARDS-1963-A

References

[1] Smelt, R., Rep. No. Aero 2081 Brit RAE Aug. (1945).

[2] Stollery, J.L. and Murthy, A.V., Aeronautical, quarterly 259 (1977).

[3] Curt, Nelander, Proceedings of the first International Symposium on Cryogenic Wind Tunnel 3-5 April (1979).

[4] Lian Qixiang, Journal of Aerodynamics, 1 (1981).

[5] Refrigeration and Cryogenic Technology, edited by Jiaotong University in Xian, 1981.

[6] Manual of Deep Refrigeration, edited by the Fourth Institute of Design of the Ministry of Chemical Engineering Vol. 2 (1979).

[7] C.R. Gales, Cryogenics, Higher Education Publishing Co., (1957).

Abstract

In order to achieve the full scale Reynolds number of aerocraft in model testing, various high-Reynolds transonic wind tunnels are being developed abroad. In this paper, a cryogenic high-Reynolds number transonic wind tunnel with pre-cooled and restricted flows is presented. The principle that air temperature falls down through a flow restrictor, which is also a regulator, is applied. Air from compressor is first cooled to 215°K, and then enters into the pressure vessels. During the wind tunnel operation, the regulating valve must be controlled, so that fluid pressure is 5atm and its temperature is 154°K. Under the different Mach number condition, the different temperature and pressure may be used to achieve a Reynolds number as high as 16.7×10^7. In this paper, the cool-system of the wind tunnel, the tunnel operating principles are described in detail, as well as the 2.4m transonic wind tunnel scheme.

END

FILMED

1-86

DTIC